

PX 930.072 / 1

he
ry
an
ry
re
an
ts
al
ty
ts
d
m
ill
ir
it
r-
3S
y

EXPERIMENTS IN
MODERN PHYSICS

BY
Adrian C. Melissinos
ASSOCIATE PROFESSOR OF PHYSICS
UNIVERSITY OF ROCHESTER



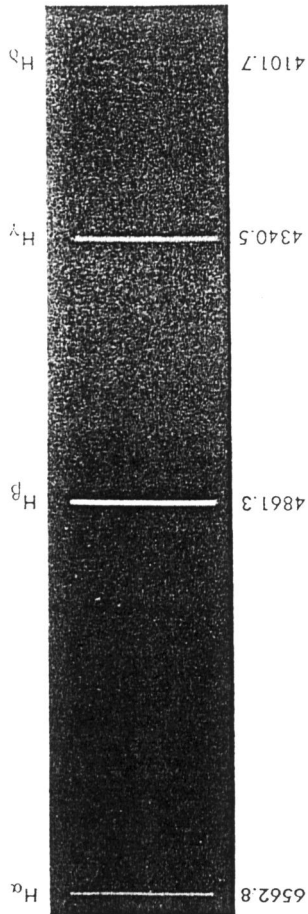


Fig. 2.9 A spectrogram of the first four lines of the Balmer series of hydrogen as obtained with the constant-deviation spectograph.

Now Eqs. 3.3 may be applied to the above data, and from the first group of helium lines, we obtain

$$\begin{aligned} A &= 2.5799 \times 10^{-6} \\ B &= 1.38655 \times 10^{-4} \\ C &= -3.3833 \end{aligned}$$

so that Eq. 3.2 yields

$$\lambda_1 = 6564.3 \text{ Å}$$

From the second group of helium lines, we obtain

$$\begin{aligned} A &= 2.7104 \times 10^{-6} \\ B &= 1.1798 \times 10^{-4} \\ C &= -5.3347 \end{aligned}$$

and thus

$$\lambda_2 = 4859.8 \text{ Å} \quad \lambda_3 = 4344.2 \text{ Å} \quad \lambda_4 = 4136.4 \text{ Å}$$

where it should be noted that λ_4 cannot be expected to be very accurate, since it lies outside the three standard helium lines d_4 , d_5 , d_6 .

As was done in section 2.3 a least-squares fit is made to obtain the best value of the Rydberg, through Eq. 1.3a

$$\frac{1}{\lambda_i} = R_H \left(\frac{1}{4} - \frac{1}{n_i^2} \right) \quad (1.3a)$$

by using only λ_1 , λ_2 , and λ_3 we obtain†

$$R_H = (1.0974 \pm 0.0014) \times 10^5 \text{ cm}^{-1}$$

in good agreement with the accepted value of

$$R_H = 1.096778 \times 10^5 \text{ cm}^{-1}$$

Thus we conclude that it is possible to obtain accuracies of the order of a few parts in 10^4 . Figure 2.9 is a reproduction of the hydrogen spectrum (as obtained by a student†) showing the first four lines of the Balmer series.

4. The Sodium and Mercury Spectrum

4.1. GENERAL

Mention has been made in the previous section of the spectrum of sodium (Na) and mercury (Hg); a brief analysis will be given here, since both elements have been investigated in detail and are representative of the one-electron and two-electron spectra. Sodium has 11 electrons, so that the $n = 1$ and $n = 2$ shells are completely filled and one electron ($n = 3$) exists outside closed shells. In this respect the sodium spectrum should be equivalent to that of hydrogen except for the central charge that the free electron sees. Indeed, since the nucleus with $Z = 11$ is "screened" by 10 negative charges (the $n = 1$ and $n = 2$ electrons) the free electron sees a potential $-e/r$ when far from the nucleus and a potential $(-Ze)/r + C$ when close to it, where C is the potential generated at the nucleus by the other electrons. However, whereas in hydrogen only one energy level was found for each value of n , a more complex situation arises in sodium, with several levels corresponding to the same n . This splitting is to be attributed to the fact that the time-independent Schrödinger equation for the hydrogen-like atom,

$$\nabla^2 \psi + \frac{2m}{\hbar^2} (E - V) \psi = 0$$

admits solutions with a principal quantum number n , and angular momentum quantum number l , such that $n \geq l + 1$; when the potential that the electron sees is exactly of the Coulomb type (as in the case of hydrogen, $V = (-Ze^2)/r$) the energy eigenvalues

$$E_n = \frac{1}{2} \frac{Z^2 e^4}{(4\pi\epsilon_0)^2 \hbar^2 n^2} \frac{m}{l} \quad (1.2)$$

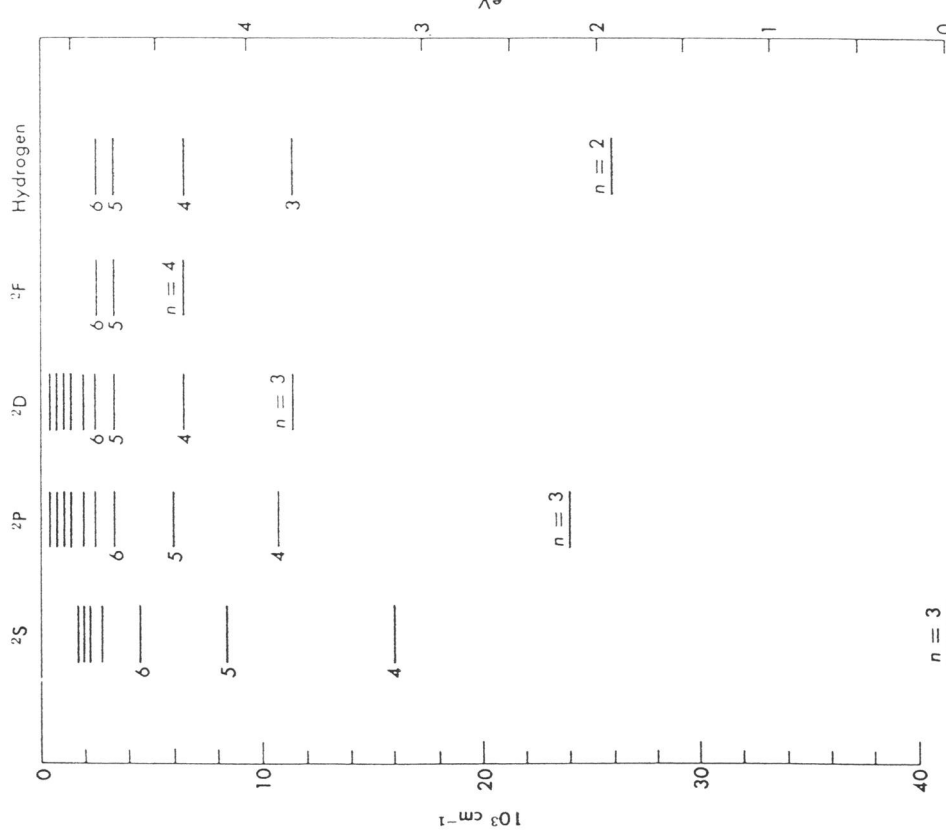
are independent of l , and agree with the Bohr theory. However, the screened potential that the free electron sees is no longer of the simple Coulomb type, and the energy of the level depends on both n and l . Orbit with smaller values of l are expected to come closer to the nucleus and thus be bound with greater strength; as a consequence their energy will be

† Ch. Georgala, class of 1963 G.

† This is the so-called Coulomb degeneracy: a peculiar coincidence for the Coulomb

depressed. The energy level diagram of sodium is shown in Fig. 2.10, where the levels have been grouped according to their l value. The customary notation is used, namely:

- $l = 0$ S state
- $l = 1$ P state
- $l = 2$ D state
- $l = 3$ F state
- $l = 4$ G state, and so on, alphabetically.



The last column in Fig. 2.10 gives the position of the levels of a hydrogen-like atom.

We note that the higher the value of l , the smaller the departures from the hydrogen-like levels (as suggested qualitatively previously) and that for given l the energy levels for different n 's follow the same ordering as the hydrogen-like atom, but with an effective charge Z^* , which for sodium is as follows:

s states	$Z^* \sim 11/9.6$
p states	$Z^* \sim 11/10.1$
d states	$Z^* \sim 1$
f states	$Z^* \sim 1$

4.2 SELECTION RULES

As we know, the spectral lines that we observe are due to transitions from one energy state to a lower one; however, in analyzing the spectrum of sodium, it becomes immediately evident that not all possible transitions occur. Thus certain "selection rules" for atomic transitions must be operative and it is found that for all spectral lines†

$$(4.1) \quad \Delta l = \pm 1$$

This selection rule is readily explained by the quantum-mechanical theory of radiation; it then means that only "electric dipole" transitions occur. Indeed, the transition probability for "electric dipole" is larger by a factor of $(c/v)^2$ (c , velocity of light) from the next order, while under no conditions a transition can be had in which the angular momentum does not change at all ($\Delta l = 0$).

By applying the selection rule of Eq. 4.1 to the energy-level diagram of Fig. 2.10, we obtain Fig. 2.11, which gives the principal lines of the sodium spectrum; since l must change by one unit, transitions will always occur between adjacent columns and never within the same one.

Figure 2.12 is a reproduction of the visible part of the above spectrum obtained by a student‡ with the constant deviation spectrograph. Beginning from the left (long wavelengths) we recognize the following lines:

- (a) Red $6154.3 - 6160.7 \text{ \AA}$
- (b) Yellow $5890.0 - 5895.9 \text{ \AA}$

¹ Exceptions (as quadrupole transitions) are found in stellar spectra.
[‡] Ch. Georgalas, Class of 1963G.

LINE

In the data above two wavelengths were given for each sodium line. Indeed, by viewing through the constant deviation or the grating spectrometer it is easy to resolve into a doublet each of the lines that appear in Fig. 2.12; the spacing is of the order of a few angstroms.

- | | | | | |
|-----|-------------|--------|---------|--------------|
| (c) | Green | 5682.7 | 5688.2 | \AA |
| (d) | | 5149.1 | -5153.6 | \AA |
| (e) | | 4978.6 | -4982.9 | \AA |
| (f) | Blue | 4748.0 | -4751.9 | \AA |
| (g) | | 4664.9 | -4688.6 | \AA |
| (h) | Blue-Violet | 4494.3 | -4497.7 | \AA |

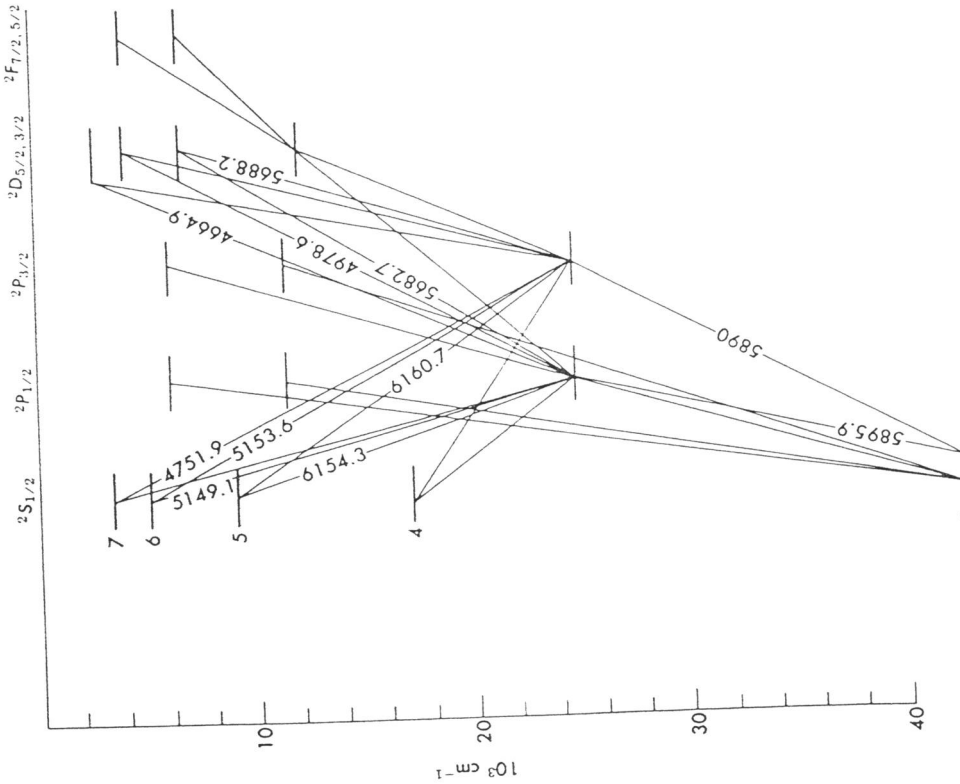


Fig. 2.11 The "allowed" transitions between the energy levels of sodium. The wavelengths in Angstroms of some of the principal lines are indicated. Note that the P states have now been shown in two columns, one referred to as $P_{1/2}$, the other as $P_{3/2}$; the small difference between their energy levels is the "fine structure."

卷之三

In the data above two wavelengths were given for each sodium line. Indeed, by viewing through the constant deviation or the grating spectrometer it is easy to resolve into a doublet each of the lines that appear in Fig. 2.12; the spacing is of the order of a few angstroms.

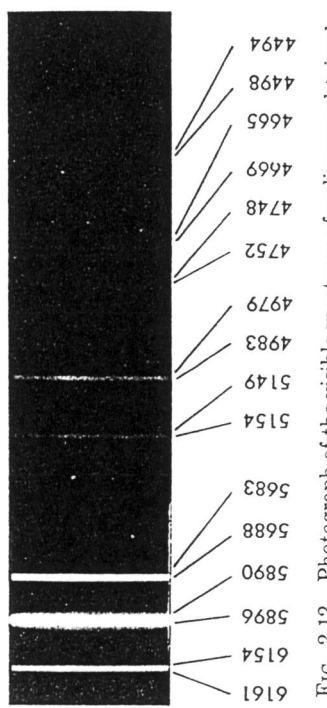


FIG. 2.12 Photograph of the visible spectrum of sodium as obtained with the constant-deviation spectrograph.

The data in Table 2.4 on the red, yellow, and green lines of sodium, viewed with the grating, were obtained by a student simultaneously with the data used for the determination of d (Section 2.2 above):

To reduce the data we note from Eq. 2.1 that

$$n_k \lambda = d(\sin \theta_k - \sin \theta_i)$$

TABLE 2.4
DATA ON THE FINE STRUCTURE OF SODIUM AS OBTAINED WITH THE SMALL GRATING
SPECTROMETER

Line	Order	θ_1	θ_2	$\Delta\theta$ (in radians)
Red	2	41°27'	41°29'	5.8×10^{-4}
	3	55°58'	56°00'	5.8
Yellow	2	40°21'	40°23'	5.8
	3	53°49'	53°52'	8.7
Green	4	75°15'	75°23'	23.2
	2	39°32'	39°33'	2.9
	4	70°48'	70°56'	23.2

[†] R. S. Stevens, class of 1963.

where θ_1 is the angle of incidence. Also

$$\theta_2 = \theta_1 + \Delta\theta$$

By letting $\sin \Delta\theta_k \simeq \Delta\theta_k$; $\cos \Delta\theta_k \simeq 1$,

$$n_k(\Delta\lambda) = d(\cos \theta_k) \Delta\theta_k \quad (4.2)$$

Using $d = 36,921 \text{ \AA}$ and averaging over orders within each line

$$\Delta\lambda = d \frac{\sum \cos \theta_k \Delta\theta_k}{\sum n_k} \quad (4.3)$$

we obtain for $\Delta\lambda$:

Line	$\Delta\lambda$ (Experiment)	$\Delta\lambda$ (Exact value)
Red	5.7 Å	6.51 Å
Yellow	6.3 Å	5.97 Å
Green	5.9 Å	5.55 Å

The experimental data are thus in fair agreement with the exact values.

This splitting of spectral lines was named "fine structure" and must reflect a splitting of the energy levels of sodium; if we express the wavelengths of sodium given in Section 4.2 in wave numbers, ($\bar{\nu} = 1/\lambda = \nu/c$) (in a scale proportional to energy), it becomes evident that the spacing in all doublets is exactly the same and equal to 17.3 cm^{-1} . Indeed, the doublet structure of all the above lines is due to the splitting of only the $3P$ ($n = 3, l = 1$) level as can be seen by referring back to Fig. 2.11. As we now know, the splitting of the $3P$ level is due to the effect of the electron "spin" and its coupling to the orbital angular momentum (designated by l). According to the Dirac theory, the electron possesses an additional degree of freedom, called the "spin," which has the properties of angular momentum of magnitude $s = \hbar/2$ (and therefore two possible orientations with respect to any axis, $m_s = +\frac{1}{2}$ or $m_s = -\frac{1}{2}$). The spin s can then be coupled to l according to the quantum-mechanical rules of addition for angular momenta; this will result in a total angular momentum of magnitude $J = l + \frac{1}{2}$ or $J = l - \frac{1}{2}$ and the energy of the state will depend on J . In the case of sodium, the $3P$ level splits into two levels, with $J = \frac{1}{2}$ and $J = \frac{3}{2}$ designated as $3P_{1/2}$ and $3P_{3/2}$ and separated by 17.3 cm^{-1} .

4.4 ELECTRON-ELECTRON COUPLING; THE MERCURY SPECTRUM

The mercury atom has $Z = 80$, hence 80 electrons; these fill shells $n = 1, n = 2, n = 3$, and $n = 4$ completely—(60 electrons) and in addition, from the $n = 5$ shell, the $l = 0, 1, 2$ subshells account for another 18 electrons. The remaining two electrons instead of occupying the $l = 3$

and $l = 4$ subshells are in the $n = 6$ shell with $l = 0$, giving rise to a configuration exactly equivalent to that of the helium atom.

We thus have an atom with two electrons outside closed shells in contrast to the one-electron systems of the hydrogen and sodium type. In the two-electron system, we can hardly speak of the n number of the system (atom), since each electron may be in a different shell; however we can still assign a total angular momentum J to the system, which will be the resultant of the values of each of the two electrons, and (as we saw in the previous section) of their additional degree of freedom, the "spin." The addition of these four angular momenta, $\mathbf{l}_1, \mathbf{l}_2, \mathbf{s}_1, \mathbf{s}_2$ to obtain the resultant \mathbf{J} can be done in several ways; for the helium or mercury atom, the Russell-Saunders coupling scheme holds, in which \mathbf{l}_1 and \mathbf{l}_2 are coupled into a resultant orbital angular momentum \mathbf{L} and \mathbf{s}_1 and \mathbf{s}_2 into a resultant spin \mathbf{S} ; finally \mathbf{L} and \mathbf{S} are coupled to give the total angular momentum of the system \mathbf{J}^+ . Since \mathbf{s}_1 and \mathbf{s}_2 have necessarily magnitude $\frac{1}{2}$, the resultant \mathbf{S} has magnitude $S = 0$ or $S = 1$. It is customary to call the states with $S = 0$ singlets, those with $S = 1$ triplets, since when $S = 0$ for any value of L , only a single state can result, with $J = L + S = L$; when $S = 1$, however, three states can result with $J = L + S, L, L - S$, namely, $J = L + 1, L, L - 1$ (provided $L \neq 0$). In systems where energy states have total angular momentum J , the selection rules for optical transitions are different—namely,

$$\Delta L = \pm 1 \quad (4.4)$$

$$\Delta J = 0, \pm 1 \quad \text{but not } J = 0 \rightarrow J = 0, \quad (4.4)$$

and in principle no transitions between triplet and singlet states.

With these remarks in mind we consider the energy-level diagram of mercury. Since there are two electrons outside a closed shell, in the ground state they will both be in the $n = 6, l = 0$ orbit, and hence (due to the Pauli principle) must have opposite orientations of their spin, leading to $S = 0$; the spectroscopic notation is 1S_0 . For the excited states one should expect both a family of singlet states and a family of triplet states; the singlets $S = 0$, will be

$${}^1S_0 \quad \text{for } L = 0, \text{ and necessarily } J = 0$$

$${}^1P_1 \quad \text{for } L = 1, \text{ and necessarily } J = 1$$

$${}^1D_2 \quad \text{for } L = 2, \text{ and necessarily } J = 2 \text{ etc.}$$

[†] In the ensuing discussion the quantum-mechanical rules of addition of angular momentum are considered known. However, even if the student is not familiar with them, he can infer them from following carefully the development of the argument.

Note the spectroscopic notation, where the upper left index is $2S + 1$ indicating the singlet nature of the state; the capital letter indicates the total L of the system (according to the convention); and the lower right index stands for J . For the triplets, $S = 1$, and the states are

$P^3 S_1$	for $L = 0$	$J = 1$
$PP_{0,1,2}$	for $L = 1$	$J = 0, 1, 2$
$PD_{1,2,3}$	for $L = 2$	$J = 1, 2, 3$, etc.

The energy levels for mercury are shown in Fig. 2.13 with some of the strongest lines of the spectrum. It is seen that the selection rules on ΔL , and ΔJ always hold, but that transitions with $\Delta S \neq 0$ do occur. It is also to be noted that the "fine structure," that is, the splitting of the $6s6p\ ^3P$ level, is of considerable magnitude: $^3P_0 - ^3P_1 = 190 \text{ cm}^{-1}$; $^3P_1 - ^3P_2 = 460 \text{ cm}^{-1}$.

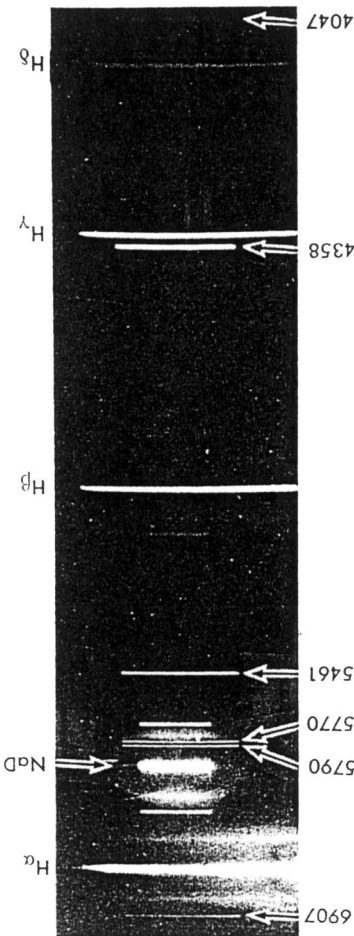
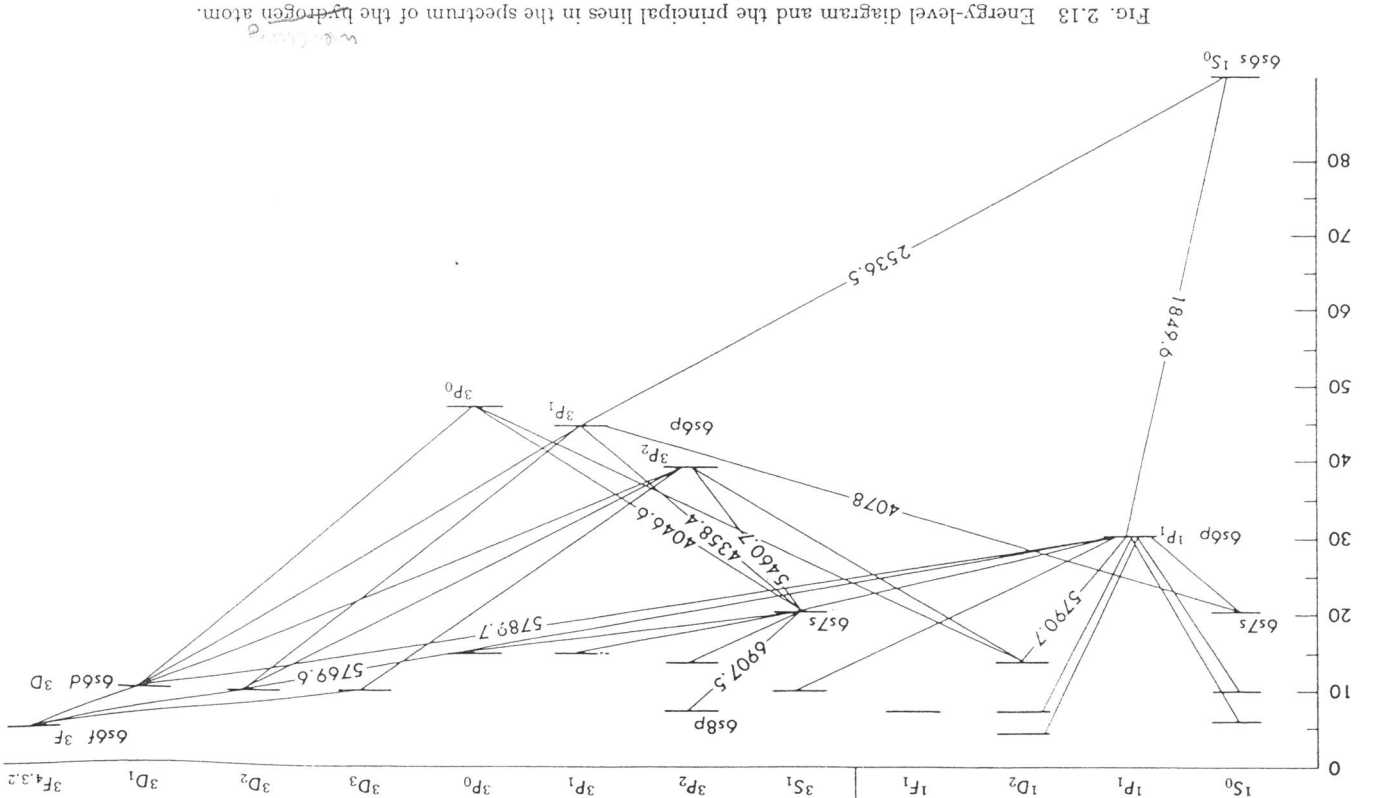


FIG. 2.14 Photograph of the superimposed spectra of hydrogen (long slit), mercury (medium slit length), and sodium (short slit).

- | | |
|--------------------|---------------|
| (a) Red | 6907.5 Å |
| (b) Yellow doublet | 5789.7–5769.6 |
| (c) Green | 5460.7 |
| (d) Blue triplet | 4358.4 |
| (e) Violet | 4046.6 |

This concludes the discussion of the spectra and energy levels of the sodium and mercury atoms. The same treatment applies to all other one-



Thus the splitting of the lines is very small and can be observed only with a high-resolution instrument. Assuming $\lambda \approx 5000 \text{ \AA}$ and $\Delta\bar{\nu} \approx 0.050 \text{ cm}^{-1}$, we find that the required resolving power is

$$\frac{\lambda}{\Delta\lambda} = \frac{\bar{\nu}}{\Delta\bar{\nu}} = 4 \times 10^9$$

Such resolution may be achieved in two ways:

(a) With a large grating used in a high order; the resolving power of a grating is given by

$$\frac{\lambda}{\Delta\lambda} = Nn$$

where n , the diffraction order, can be as large as 20, and for a 10-in. grating with 7000 rulings to the inch, the number of rulings is $N = 7 \times 10^4$, so that

$$\frac{\lambda}{\Delta\lambda} \approx 10^6$$

Such gratings, are, however, very difficult to construct, but can now be obtained commercially.

(b) With a "multiple beam" interferometer; the most common one today and easiest to use being the Fabry-Perot. It consists of two reflecting glass plates of high quality which are kept parallel and at a distance t . The interference pattern appears as a series of concentric rings, and the resolution, the so-called "instrument width" is:

$$\delta\bar{\nu} = \frac{1}{2t} \frac{1-R}{\pi\sqrt{R}} \quad (1.5a)$$

where R is the reflectivity of the plates. It is more helpful to use the expression

$$\Delta\bar{\nu} = \Delta n \frac{1}{2t} \quad (1.5b)$$

where Δn is the fraction of an order by which the ring has been shifted. It is easy to distinguish $\Delta n \sim 1/10$, and t can be as large† as 2 cm, so that

$$\Delta\bar{\nu} = 25 \times 10^{-3} \text{ cm}^{-1}$$

which for $\lambda = 4000 \text{ \AA}$ corresponds to $\lambda/\Delta\lambda \approx 10^6$. An additional require-

† In special cases connected with the observation of lasers, spacings as large as 1 m have been used.

ment for the observation of such small structure of spectral lines is that the lines themselves be narrower than the spacing between the components of the structure. For that purpose special light sources have been constructed which emit lines that are as narrow as possible.

In this chapter we first present an elementary discussion of the theory of the Zeeman effect and of the theory of hyperfine structure. A brief section is devoted to light sources, and next the Fabry-Perot interferometer is described. In Section 6, experimental data on the Zeeman effect of the 5461-Å green line of Hg^{1s} , obtained with a Fabry-Perot, are treated in detail. Next, the medium-resolution grating spectrograph used in this laboratory is described and data on the Zeeman effect obtained with it, are presented; finally data on the hyperfine structure of mercury obtained with a grating of high quality are also presented.

REFERENCES

By necessity the discussion of certain topics in this chapter is very brief. However the bibliography on atomic spectroscopy is excellent and extensive. The following texts and monographs should be very useful to the student.

E. U. Condon and G. H. Shortley, *The Theory of Atomic Spectra*, Oxford Univ. Press. This is one of the most complete theoretical treatments on atomic spectroscopy, but at an advanced level.

H. E. White, *Introduction to Atomic Spectra*, McGraw-Hill. This book contains extensive data on atomic spectra and the treatment of the theory is based on the semi-classical approach of the vector model.
H. Kuhn, *Atomic Spectra*, Longman's, London, 1962. A recent good book on a slightly more advanced level than White's book, referred to above.

S. Tolansky, *High Resolution Spectroscopy*, Methuen, London. A very comprehensive and clear treatise on the instruments and techniques of high-resolution spectroscopy.
H. Kopfmann, *Nuclear Moments*, Academic Press. This book contains a very complete discussion of atomic hyperfine structure, of analysis methods, and of the conclusions that are obtained from it.

2. The Zeeman Effect

2.1 THE NORMAL ZEEMAN EFFECT

As already discussed in Chapter 2, Section 4, the solution of the Schrödinger equation† yields "stationary states" labeled by three integer indices, n , l , and m , where $l < n$ and $m = -l, -l+1, \dots, l-1, l$. For the screened Coulomb potential, the energy of these states depends on n and l but not on m ; we therefore say that the $(2l+1)$ states with the same

† See, for example, E. Fermi, *Notes on Quantum Mechanics*, Univ. of Chicago Press, or any other text on quantum mechanics.

n and l index are "degenerate" in the m quantum number. Classically we can attribute this degeneracy to the fact that the plane of the "orbit" of the electron may be oriented in any direction without affecting the energy of the state, since the potential is spherically symmetric.

If now a magnetic field H is switched on in the region of the atom, we should expect that the electrons (and the nucleus!) will interact with it. We need only consider the electrons outside closed shells, and let us assume there is one such electron; indeed the interaction of the magnetic field with this electron yields for each state an additional energy ΔE , given by

$$\Delta E = m\mu_0 H \quad (2.1)$$

Thus, the total energy of a state depends now on n , l , and m , and the degeneracy has been removed.



Fig. 7.1 Magnetic moment due to a current circulating in a closed loop.

To see how this additional energy arises we consider again the classical analogy. Then the orbiting electron is equivalent to a current density \mathbf{J}

$$\mathbf{J}(\mathbf{x}) = -ev \delta(\mathbf{x} - \mathbf{r})$$

where \mathbf{r} is the equation of the orbit and \mathbf{x} gives the position of the electron; the negative sign obviously arises from the negative charge of the electron. Such a current density gives rise to a magnetic dipole moment

$$\mathbf{u} = \frac{1}{2c} \int \mathbf{x} \times \mathbf{J}(\mathbf{x}) d^3x = -\frac{1}{2c} e(\mathbf{r} \times \mathbf{v})$$

[†] For our present discussion this interaction of the nucleus with the external field is so small that we will neglect it.

[‡] For a circular orbit, the electron is equivalent to a current $I = \Delta Q/\Delta T = e/T = e\omega/2\pi$ where ω is the angular frequency $\omega = v/a$; a is the radius of the orbit. But a plane closed loop of current gives rise to a magnetic moment $\mu = (I/c)A$ where A is the area enclosed by the loop; in our case $A = \pi a^2$, hence

$$\mu = \frac{ev}{2\pi ac} \pi a^2 = \frac{eva}{2c}$$

The angular momentum for the circular orbit is $L = m_e p_a$, hence as in Eq. 2.2,

$$\mu = \frac{e}{2m_e c} L$$

But the angular momentum of the orbit is given by

$$\mathbf{L} = \mathbf{r} \times \mathbf{p} = m_e(\mathbf{r} \times \mathbf{v})$$

so that

$$\mathbf{u} = -\frac{e}{2m_ec} \mathbf{L} = -\frac{eh}{2m_ec} k\mathbf{u}_L \quad (2.2)$$

where we expressed the angular momentum of the electron in terms of its quantized value (according to Bohr) $\mathbf{L} = \hbar/2\pi$ and \mathbf{u}_L is a unit vector along the direction of \mathbf{L} . Now, the energy of a magnetic dipole in a homogeneous field is

$$E = -\mathbf{u} \cdot \mathbf{H} = \frac{e}{2m_ec} \mathbf{L} \cdot \mathbf{H} \quad (2.3)$$

but the angle between \mathbf{L} and the external field \mathbf{H} cannot take all possible values.[†] We know that it is quantized, so that the projection of \mathbf{L} on the z axis (which we can take to coincide with the direction of \mathbf{H} since no other preferred direction exists) can only take the values $m = -l, -l+1, \dots, l-1, l$. Thus, the energy of a particular state n, l, m in the presence of a magnetic field will be given by[‡]

$$E_{n,l,m} = -E_{n,l} + mI\mu_0 \quad (2.4)$$

where[§]

$$\mu_0 := \frac{eh}{2m_ec}$$

In Fig. 7.2 is shown the energy-level diagram for the five states with given n and $l = 2$, before and after the application of a magnetic field H . We

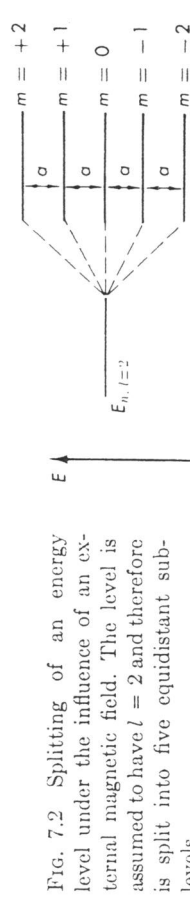


Fig. 7.2 Splitting of an energy level under the influence of an external magnetic field. The level is assumed to have $l = 2$ and therefore is split into five equidistant sublevels.

[†] This was first clearly shown in the Stern-Gerlach experiment.

[‡] The energy in the field is $+(eh/2mc)^2$ because the electron charge is taken as negative.

[§] In the MKS system $\mu_0 = (eh/2m_e)$; m_e in this expression is obviously the mass of

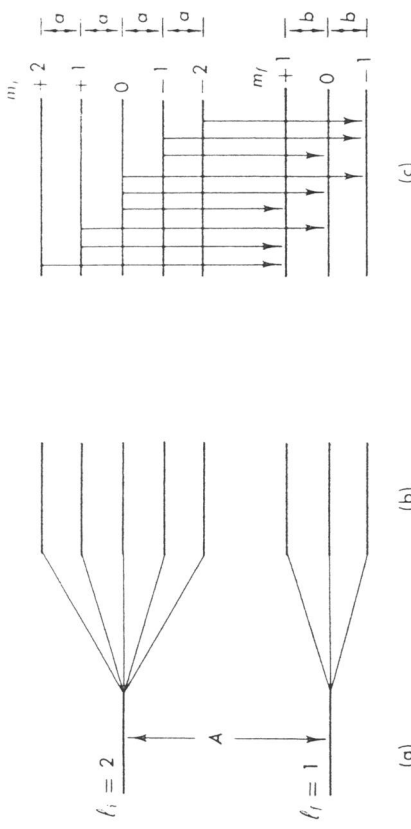


FIG. 7.3. Splitting of a spectral line under the influence of an external magnetic field. (a) The initial level ($\ell = 2$) and the final level ($\ell = 1$) with no magnetic field are shown. A transition between these levels gives rise to the spectra line. (b) The two levels after the magnetic field has been applied. (c) The nine allowed transitions between the eight sublevels of the initial and final state.

note that all the levels are equidistantly spaced, the energy difference between them being

$$\Delta E'_{\mu_0 H}$$

Let us next consider the transition between a state with n_i, ℓ_i, m_i and one with n_f, ℓ_f, m_f . As an example we choose $\ell_i = 2$ and $\ell_f = 1$, and the energy-level diagram is shown in Fig. 7.3, without a magnetic field in Fig. 7.3a, and when the magnetic field is present in Fig. 7.3b.

However, we know that for an electric dipole transition to take place between two levels, certain selection rules must be fulfilled: in particular,

$$\Delta l = \pm 1 \quad (2.5)$$

Thus, when the field is turned on, we cannot expect transitions between the m sublevels with the same l , since they do not satisfy Eq. 2.5. Further, also the transitions between the sublevels with $\ell_i = 2$ to the sublevels with $\ell_f = 1$ which do satisfy Eq. 2.5 are now governed by the additional selection rule†

$$\Delta m = 0, \quad \pm 1 \quad (2.6)$$

and thus only the transitions shown in Fig. 7.3c are allowed.

Let the energy splitting in the initial level be A , and in the final level be b , and let Δ be the energy difference between the two levels when no

TABLE 7.1
ALLOWED TRANSITIONS FROM $\ell_i = 2$ TO $\ell_f = 1$ AND THE CORRESPONDING ENERGIES

		m of initial state				
		+2	+1	0	-1	-2
m of final state		+2	+1	0	-1	-2
+1		$A + 2a - b$	$A + a - b$	$A - b$	\times	\times
0		\times	$A + a$	A	$A - a$	\times
-1		\times		$A + b$	$A - a + b$	$A - 2a + b$

Note: An \times indicates that this particular transition may not take place.

magnetic field is applied. Then the energy released in a transition $i \rightarrow f$ is given by

$$E_i - E_f = A_{if} + m_i a - m_f b \quad (2.7)$$

These energy differences for the nine possible transitions shown in Fig. 7.3c, are given in matrix form in Table 7.1; an \times indicates that the transition is forbidden and will not take place.

At this point the reader must be concerned about the use of a and b ; according to our previous argument (Eq. 2.4), as long as all levels are subject to the same magnetic field H , their splitting must also be the same, and

$$a = b = \mu_0 H$$

Thus, we see from Eq. 2.7 (or Table 7.1) that only three energy differences are possible

$$E_i - E_f = A + (m_f - m_i) = A + a \Delta m$$

where Δm is limited by the selection rule, Eq. 2.6, to the three values $+1, 0, -1$. Consequently, in the presence of a magnetic field H , the single spectral line of frequency $\nu = A/h$ is split into three components with frequencies

$$\nu_- = (A - \mu_0 H)/h, \quad \nu_0 = A/h, \quad \text{and} \quad \nu_+ = (A + \mu_0 H)/h$$

irrespective of the values of ℓ_i and ℓ_f . Furthermore, these spectral lines are polarized, as shown in Fig. 7.4. When the Zeeman effect is viewed in a direction normal to the axis of the magnetic field, the central component is polarized parallel to the axis whereas the two outer ones normal to the axis of the field. When the Zeeman effect is observed along the axis of the field (by making a hole in the pole face, or using a mirror), only

† The selection rules of atomic spectroscopy are a consequence of the addition of angular momenta. In this specific case, the selection rules indicate that we consider only

$\Delta m = +1$ transitions appear with right-hand circular polarization; from $\Delta m = -1$ transitions, with left-hand circular polarization. The central line does not appear, since the electromagnetic field must always have the field vectors (\mathbf{E} and \mathbf{B}) normal to the direction of propagation.

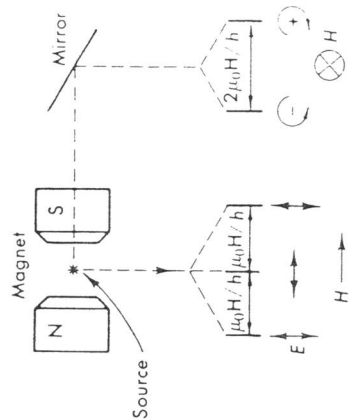


Fig. 7.4 The polarization and separation of the components of a normal Zeeman multiplet when viewed in a direction normal to, and in a direction parallel to, the magnetic field.

The splitting of a spectral line into a triplet under the influence of a magnetic field is called the ‘normal’ Zeeman effect, and is occasionally observed experimentally, as, for example, in the 5790 Å line of mercury arising in a transition[†] from 1D_2 to 1P_1 . But in most cases the lines are split into more components, and even where a triplet appears it does not always show the spacing predicted by Eq. 2.4. This is due to the intrinsic magnetic moment of the electron (associated with its spin) and will be discussed in the following sections.

2.2 THE INFLUENCE OF THE MAGNETIC MOMENT OF THE ELECTRON

In Chapter 2 it was discussed how the intrinsic angular momentum (spin) of the electron \mathbf{S} couples with the orbital angular momentum of the electron \mathbf{L} to give a resultant \mathbf{J} ; this coupling gave rise to the ‘fine structure’ of the spectra.[‡] The projections of \mathbf{J} on the z axis are given by m_J and we could expect (on the basis of our previous discussion) that the total magnetic moment of the electron will be given by

$$\mathbf{u} = \frac{\mu_0}{\hbar} \mathbf{J} \quad (2.8)$$

[†] Note that both initial and final state have $S = 0$.

[‡] We will use the following notation: $\mathbf{L}, \mathbf{S}, \mathbf{J}$ represent the angular momentum vectors which have magnitude $\hbar\sqrt{s(s+1)}, \hbar\sqrt{s(s+1)}, \hbar\sqrt{j(j+1)}$. The symbols l, j , etc. (s is always $s = \frac{1}{2}$) are the quantum numbers which label a one-electron state and appear in the above square root expressions.

The symbols L, S, J , etc., are the quantum numbers which label a state with more than one electron and one h -bar spin quantum number.

Consequently, the energy-level splitting in a magnetic field H would be in analogy to Eq. 2.4,

$$\Delta E = -m_J \mu_0 H \quad (2.9)$$

These conclusions, however, are not correct because the *intrinsic* magnetic moment of the electron is related to the *intrinsic* angular momentum of the electron (the spin) through

$$\mathbf{u}_e = 2 \frac{e}{2m_e c} \mathbf{S} = 2 \frac{e\hbar}{2m_e c} s \mathbf{u}_s \quad (2.10)$$

and *not* according to Eq. 2.2.[†] Consequently, the *total* magnetic moment of the electron is given by the operator

$$\mathbf{u} = (\mu_0/\hbar)[\mathbf{L} + 2\mathbf{S}] \quad (2.11)$$

We can think of it as a vector oriented along \mathbf{J} but of magnitude

$$\mu = \mu_0 g J \quad (2.12)$$

The numerical factor g is called the Landé g factor and a correct quantum-mechanical calculation gives:[‡]

$$g = 1 + \frac{j(j+1) + s(s+1) - l(l+1)}{2j(j+1)} \quad (2.13)$$

[†] The result of Eq. 2.10 is obtained in a natural way from the solution of the Dirac equation; also from the classical relativistic calculation of the ‘Thomas precession.’

[‡] This result can also be obtained from the vector model for the atomic electron. In Fig. 6.5 the three vectors \mathbf{J} , \mathbf{L} , and \mathbf{S} are shown, and \mathbf{L} and \mathbf{S} couple into the resultant \mathbf{J} , so that

$$\mathbf{J} = \mathbf{L} + \mathbf{S}$$

By taking the squares of the vectors, we obtain the following values for the cosines

$$\cos(\mathbf{L}, \mathbf{J}) = \frac{j^2 + l^2 - s^2}{2lj} \quad \cos(\mathbf{S}, \mathbf{J}) = \frac{j^2 + s^2 - l^2}{2sj}$$

From Eq. 2.11 we see that

$$\mu/\mu_0 = l \cos(\mathbf{L}, \mathbf{J}) + 2s \cos(\mathbf{S}, \mathbf{J})$$

Thus

$$g = \frac{\mu}{\mu_0} = \frac{j^2 + l^2 - s^2}{2lj} + \frac{2j^2 + 2s^2 - 2l^2}{2sj} = 1 + \frac{j^2 + s^2 - l^2}{2sj} \quad \text{Fig. 7.5 Addition of the orbital angular momentum } \mathbf{L}, \text{ and of the spin angular momentum } \mathbf{S} \text{ into the total angular momentum } \mathbf{J}, \text{ according to the vector model.}$$

Finally we must replace j^2 , s^2 , and l^2 by their quantum mechanical expectation values in Eq. 2.13, etc., and we obtain Eq. 2.13.

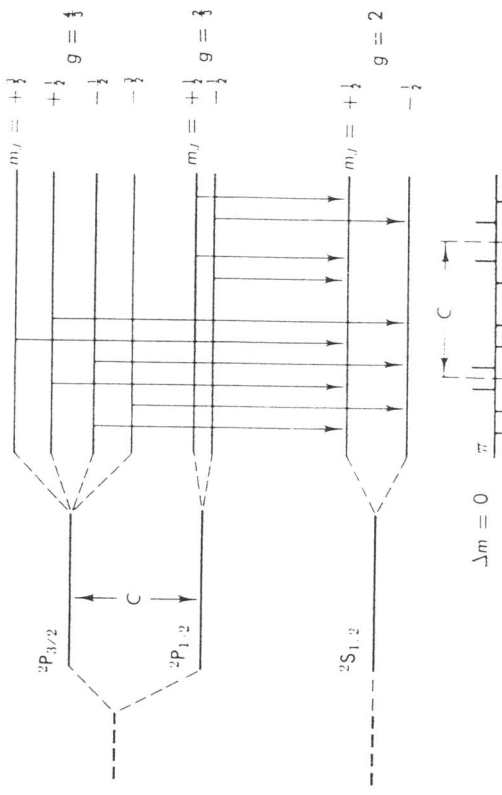


Fig. 7.6 Energy levels of a single valence electron atom showing a P state and an S state. Due to the fine structure, the P state is split into a doublet with $j = \frac{3}{2}$ and $j = \frac{1}{2}$. Further, under the influence of an external magnetic field each of the three levels is split into sublevels as shown in the figure where account has been taken of the magnetic moment of the electron. The magnetic quantum number m_j for each sublevel is also shown as is the g factor for each level. The arrows indicate the allowed transitions between the initial and final states, and the structure of the line is shown in the lower part of the figure.

The interesting consequence of Eqs. 2.12 and 2.13 is that now the splitting of a level due to an external field H is

$$\Delta E = (g\mu_0 H)m_j \quad (2.14)$$

and in contrast to Eq. 2.4 is *not* the same for all levels; it depends on the j and l of the level ($s = \frac{1}{2}$ always when one electron is considered). The sublevels are still equidistantly spaced but by an amount

$$\Delta E = g\mu_0 H$$

Let us then consider again the transitions between sublevels belonging to two states with different l (in order to satisfy Eq. 2.5). Since, however, we are taking into account the electron spin, l is not a good quantum number, and instead the j values of the initial and final level must be specified. If we choose for this example $l_i = 1$ and $l_f = 0$, we have the choice of $j_i = \frac{3}{2}$ or $j_i = \frac{1}{2}$, whereas $j_f = \frac{1}{2}$. Transitions may occur only if they satisfy, in addition to Eq. 2.5, also the selection rules for j

Furthermore the selection rules for m_j must also be satisfied; they are the same as given by Eq. 2.6

$$\Delta m_j = 0, \pm 1 \quad (2.6a)$$

In Fig. 7.6 the energy-level diagram is given without and with a magnetic field for the doublet initial state with $l = 1$ and the singlet final state, $l = 0$. Six possible transitions between the initial states with $j = \frac{3}{2}$ to the final state with $j = \frac{1}{2}$ are shown (as well as the four possible transitions from $j = \frac{1}{2}$ to $j = \frac{1}{2}$). By using Eq. 2.13 we obtain the following g factors

$$\begin{array}{llll} l = 1 & j = \frac{3}{2} & s = \frac{1}{2} & g = \frac{4}{3} \\ l = 1 & j = \frac{1}{2} & s = \frac{1}{2} & g = \frac{2}{3} \\ l = 0 & j = \frac{1}{2} & s = \frac{1}{2} & g = 2 \end{array}$$

The sublevels in Fig. 7.6 have been spaced accordingly.

TABLE 7.2
ALLOWED TRANSITIONS FROM $j_i = \frac{3}{2}$ TO $j_f = \frac{1}{2}$ AND THE CORRESPONDING ENERGIES

m_j of final state	$+ \frac{3}{2}$	$+ \frac{1}{2}$	$- \frac{1}{2}$	$- \frac{3}{2}$
ΔE	$A + \frac{3a}{2} - \frac{b}{2}$	$A + \frac{a}{2} - \frac{b}{2}$	$A - \frac{a}{2} - \frac{b}{2}$	$A - \frac{3a}{2} + \frac{b}{2}$
\times	\times	\times	\times	\times

In Table 7.2 are now listed the six transitions from $j = \frac{3}{2}$ to $j = \frac{1}{2}$ in analogy with Table 7-1. However, since now $a \neq b$, the spectral line is split into a six-component (symmetric) pattern. This structure of the spectral line is indicated in the lower part of Fig. 7.6; following adopted convention, the components with polarization parallel to the field are indicated above the base line, and with normal polarization below.[†] As before the parallel components have $\Delta m = 0$, the normal ones $\Delta m \pm 1$.

The horizontal spacing between the components is proportional to the differences in the energy of the transition, and the vertical height is proportional to the parallel components with π , and the normal

[†] It is also conventional to label the parallel components with π , and the normal

portional to the intensity of the components; the relative intensity can be predicted exactly since it involves only the comparison of matrix elements between the angular parts of the wave function.

As the magnetic field is raised, the separation of the components continues to increase linearly with the field until the separation between Zeeman components becomes of the order of the fine-structure separation (spacing C in Fig. 7.6). At this point the Zeeman components from the $j = \frac{3}{2} \rightarrow \frac{1}{2}$ and $j = \frac{1}{2} \rightarrow \frac{1}{2}$ transition begin to overlap; clearly the perturbation caused by the external magnetic field is of the order of the $\mathbf{L} \cdot \mathbf{S}$ energy and affects the coupling of \mathbf{L} and \mathbf{S} into \mathbf{J} ; \mathbf{J} ceases to be a "good quantum number."

For very strong fields, \mathbf{L} and \mathbf{S} become completely uncoupled, so that the orbital and intrinsic magnetic moments of the electron interact with the field independently, giving rise to an energy shift

$$\Delta E = -\frac{\mu_0}{\hbar} \mathbf{L} \cdot \mathbf{H} = 2 \frac{\mu_0}{\hbar} \mathbf{S} \cdot \mathbf{H} - a \mathbf{L} \cdot \mathbf{S}$$

$$= -\mu_0 H (m_l + 2m_s) - a m_l m_s \quad (2.15)$$

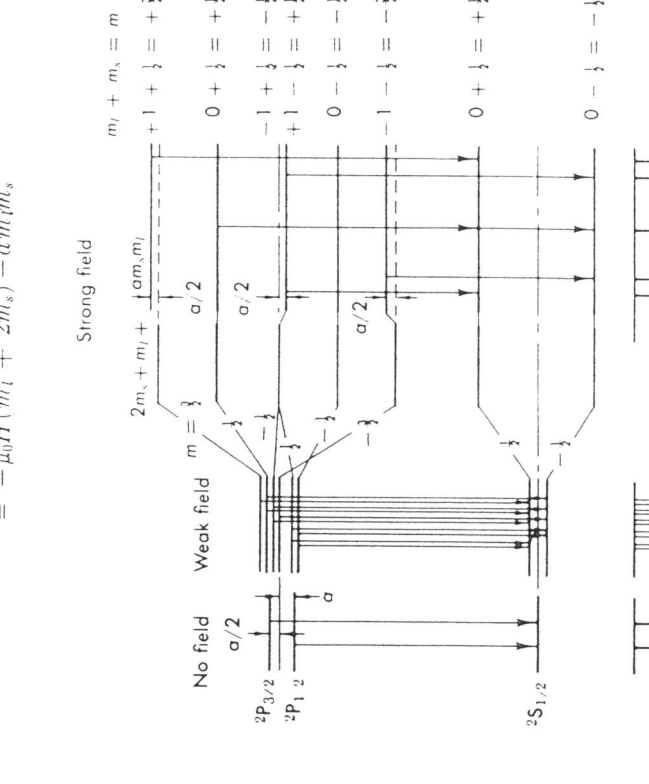


Fig. 7.7 Energy levels that are the same as Fig. 7.6 but include the region of very strong magnetic field. Note how the sublevels belonging to the $j = \frac{3}{2}$ and $j = \frac{1}{2}$ levels cannot any more be distinguished but have coalesced into five components typical of Fig. 7.2.

Here, m_l and m_s are the projections of \mathbf{L} and \mathbf{S} on the z axis, and in this case the selection rules for electric-dipole transitions become

$$\Delta m_l = 0, \pm 1 \quad \text{and} \quad \Delta m_s = 0 \quad (2.16)$$

In Fig. 7.7 the splitting of the six Zeeman sublevels for the $l = 1, s = \frac{1}{2}$ fine-structure doublet is shown for a weak and for a strong external magnetic field. For weak fields we have the situation already shown in Fig. 7.6 (Eq. 2.14) while in the limit of very strong fields the six sublevels coalesce into five components almost equidistantly split as predicted by Eq. 2.15. However, an additional term must be added to take account of the $\mathbf{L} \cdot \mathbf{S}$ interaction, which even though weak is still present. As a result, the structure of the spectral line becomes almost a normal Zeeman triplet, as can also be seen in Fig. 7.7. This phenomenon is called the Paschen-Back effect. It necessitates, however, magnetic fields that are beyond the reach of iron core magnets, and thus are difficult to achieve.

2.3 ATOMS WITH MORE THAN ONE VALENCE ELECTRON

In the previous section we discussed the Zeeman effect, including the electron's spin, but only for the case of one (valence) electron outside a closed shell. We have, however, considered in Chapter 2 (Section 4.4) the coupling of the orbital angular momenta $\mathbf{l}_1, \mathbf{l}_2, \dots$ of the valence electrons into a resultant \mathbf{L} , and of their spins $\mathbf{s}_1, \mathbf{s}_2, \dots$, into a resultant \mathbf{S} , which then couple to give $\mathbf{J} = \mathbf{L} + \mathbf{S}$. This is the so-called Russell-Saunders coupling and is applicable to mercury; the energy-level diagram and a discussion of the mercury spectrum were given in Chapter 2 (Fig. 2.13).

Let us consider the familiar 5461 Å green line which arises from a transition between the $^3S_1(6s7s)$ state to the $^3P_2(6s6p)$ state. Using Eq. 2.13 we can obtain the g factors for the initial and final state:[†]

$$^3S_1(J = 1, L = 0, S = 1) \quad g_i = 2 \quad (2.16)$$

$$^3P_2(J = 2, L = 1, S = 1) \quad g_f = \frac{3}{2}$$

In Fig. 7.8 is given the energy-level diagram for these two states without and with a magnetic field. The structure of the line is indicated in the lower part of the figure and exhibits a symmetric nine-component pattern.

Indeed, the example we are considering involves the same angular momentum $l_i = 1, l_f = 2$ as the example discussed in Section 2.1, where we concluded that only three components would appear because of the equality of the splitting a of the initial level, and of the splitting b , of the final level angular momenta of the two valence electrons.

[†] Note that we use in Eq. 2.13 L, S , and J , the quantum numbers for the coupled angular momenta of the two valence electrons.

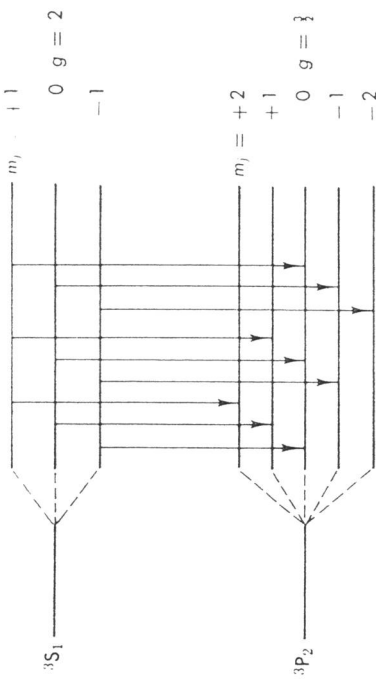


FIG. 7.8. Structure of the Zeeman multiplet arising in a transition from a 3S_1 to a 3P_2 line; the mercury green line at 5461 \AA is an example of such a transition. Note that the situation here is similar to that indicated in Fig. 7.3 if the initial and final state are interchanged.

$$\Delta m = 0 \quad \pi = 2 - 1 \downarrow 1 \quad 1 \quad 2 \quad \Delta \bar{\nu} \text{ in units of } (\mu_0 H / h)$$

$$\Delta m = \pm 1 \quad \sigma = -\frac{1}{2} - \frac{1}{2} \quad 0 \quad \frac{1}{2}$$

where M is the mass of the nucleus. In addition, nuclei exhibit an intrinsic magnetization†, so that in general we have

$$\mathbf{u} = -g_I \frac{e}{2m_p c} \mathbf{I} = g_I \mu_N I \mathbf{u}_I$$

where \mathbf{u}_I is a unit vector along the spin direction, and

$$\mu_N = \frac{e\hbar}{2m_p c}$$

is the nuclear magneton; m_p is the proton mass. The numerical factor g_I includes all the effects of intrinsic and orbital magnetization of the nucleus and can be obtained only from a theory of nuclear structure.

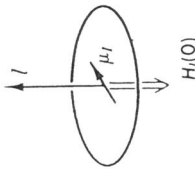


FIG. 7.9. Interaction of the nuclear magnetic moment with the magnetic field $\mathbf{H}_e(0)$ produced by the atomic electrons at the nucleus.

Clearly, such a magnetic moment of the nucleus, \mathbf{u} , will interact with the magnetic field $\mathbf{H}_e(0)$ produced by the atomic electrons (at the nucleus; Fig. 7.9). This interaction then results in a shift of the energy levels of the atom (electrons + nucleus, system) by the amount

$$\Delta E = -\mathbf{u} \cdot \mathbf{H}_e(0) \quad (3.3)$$

The direction of $\mathbf{H}_e(0)$ is that given by the total angular momentum of the atomic electrons, namely, \mathbf{J} ,‡ so that

$$\Delta E = +\left(\frac{\mu}{|I|}\right)\left(\frac{H_e(0)}{|J|}\right)\mathbf{I} \cdot \mathbf{J} \quad (3.4)$$

Thus, we expect the splitting of a level of given J according to the possible values of $(\mathbf{I} \cdot \mathbf{J})$ which as we know are quantized. As a matter of fact, the situation is analogous to that of the fine structure, where the interaction was proportional to the $(\mathbf{L} \cdot \mathbf{S})$ term. In that instance the two angular action was proportional to the $(\mathbf{L} \cdot \mathbf{S})$ term. In that instance the two angular momenta coupled into a resultant $\mathbf{J} = (\mathbf{L} + \mathbf{S})$ according to the quantum-mechanical laws of addition of angular momentum. In the present situation

† This gives rise to the so-called "anomalous" magnetic moment of the nucleon; for example, the neutron (an uncharged particle) has a magnetic moment of $-1.91 \mu_N$.
‡ The direction of $\mathbf{H}_e(0)$ is really opposite to \mathbf{J} because the electron has negative charge.

(Table 7.1). However, in the present instance, the different g factors (Eq. 2.16) make $a \neq b$ and give rise to all nine components; the experimental data obtained on the Zeeman effect of this spectral line and discussed in Section 6 below do confirm the structure predicted by Fig. 7.8.

3. Hyperfine Structure

3.1 MAGNETIC DIPOLE INTERACTION

As stated in the introduction, spectral lines, when examined under high resolution, do show a small structure even when no magnetic field is applied. It was also mentioned that such hyperfine structure is due to the interaction of the higher moments of the nucleus with the electromagnetic field of the valence electron or electrons. We will defer the more general treatment of the multipole moments of the nucleus to Section 3.4 and will first discuss only the interaction of the nuclear dipole magnetic moment.

If we consider a nucleus with an intrinsic angular momentum (spin) \mathbf{I} different from zero ($I \geq \frac{1}{2}$), we can expect that the revolving charge of the nucleus will give rise to a magnetic moment (see Eq. 2.2) oriented along the spin axis.

$$\mathbf{u} = -\frac{e}{2Mc} \mathbf{I}$$

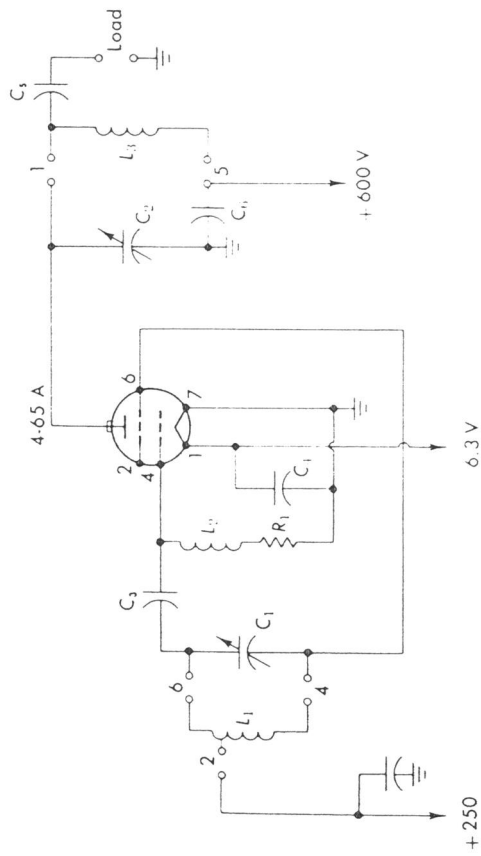


Fig. 7.15. A radio frequency oscillator suitable for exciting an electrodeless discharge tube. Such a source emits spectral lines of narrow width.

$L_1 = 20$ turns No. 16 wire $1\frac{1}{2}$ dia. $1\frac{1}{8}$ L, tapped $6\frac{1}{2}$	$C_3 = 3800 \mu\mu F$
$L_2 = 7$ turns No. 16 wire $\frac{3}{8}$ dia. $1\frac{1}{8}$ L	$C_4 = 0.02 \mu F$ 600 V
$L_3 = 7$ MC BUD-OE L-40	$C_5 = 0.01 \mu F$ 5000 V
$C_1 = 100 \mu\mu F$	$C_6 = 0.1 \mu F$ 3000 V
$C_2 = 200 \mu\mu F$	$R_1 = 5K$ 20W

possible to the natural one, but they must also be quite intense, since high-resolution instruments by necessity have small luminosity. The sources most commonly used are the hollow cathode and the electrodeless discharge.

In this laboratory the electrodeless discharge is used. It consists of a narrow tube (pyrex or quartz) containing a separated mercury isotope (198) and filled with 10 mm of neon. A radiofrequency or microwave source is coupled to it by means of clip-leads or a wave guide and provides the power for sustaining the discharge; the source usually has to be started with a spark (Tesla) coil. The source may be cooled with an air blast, or by other means, to dissipate the power absorbed by the glass envelope; Fig. 7.15 shows the 7 Mc 50-watt radiofrequency oscillator used in this laboratory to excite the source; the tuning condenser is adjusted for maximum brilliance or as desired. The Hg^{198} source operated in this fashion yielded lines of half width at half maximum of the order of $\Delta\bar{\nu} = 0.030 \text{ cm}^{-1}$.

If a quartz (or vycor) envelope is used for the source (as it must be when ultraviolet lines are investigated), the experimenter must always wear glasses. As is well known, even short exposures of the eye to ultraviolet light cause damage, sometimes permanent; strong ultraviolet mercury lines even cause sunburn of the skin.

5. The Fabry-Perot Interferometer

5.1 GENERAL DISCUSSION

As mentioned in the introduction, the Fabry-Perot is the most commonly used of the "multiple-beam" interferometers; other instruments in this category are the Lummer-Gehrcke plate and the Michelson échelon. The Fabry-Perot has found many uses, such as the measurement of refractive indices of gases, measurement of lengths, and so on, but here we will be mainly concerned with its application to the measurement of very small differences in wavelengths such as appear in the Zeeman effect and hyperfine structure.

The Fabry-Perot consists of two parallel flat glass plates, coated on the inner surface with a partially transmitting metallic layer. Consider

sorption cross section; this will be strongest in the center of the line and weaker in the wings. The result shown in Fig. 7.14a is that the line becomes "squashed" in the center; that is, it is broadened.

If now the outer layers of the source are much cooler than the middle ones, the width of the particular energy level (due to the Doppler effect) is smaller in the outer layers and absorption takes place only at the central frequency with almost none in the wings. The result is a "self-reversed" line as shown in Fig. 7.14b. This effect is very pronounced in the sodium D D-lines, and when it is viewed with a high-resolution instrument, the line exhibits a doublet structure which is frequently mistaken for hyperfine structure.

In this laboratory when a commercial high-pressure sodium light is used for the alignment of the Fabry-Perot interferometer, each D line gives rise to a double ring pattern. The separation between centers is of the order of approximately 0.100 cm^{-1} and is a function of the operating voltage, indicating that it is due to self reversal.[†]

In order to avoid these causes of spectral line broadening, special sources have been developed. They must radiate lines whose width is as close as

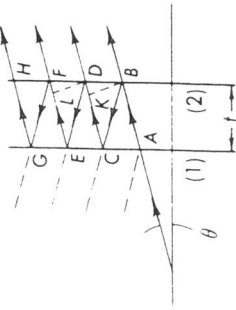


Fig. 7.16. Reflected and transmitted rays at the two parallel surfaces (1) and (2) of a Fabry-Perot etalon. The étalon spacing is t .

[†] The hyperfine structure pattern of the sodium D lines is 0.065 cm^{-1} wide.

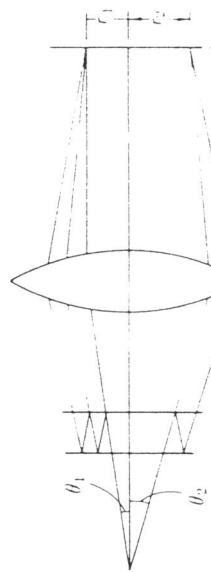


FIG. 7.17. Focusing of the light emerging from a Fabry-Perot étalon. Light entering the étalon at an angle θ is focused onto a ring of radius $r = \pi\theta$ where f is the focal length of the lens.

then, the two partially transmitting surfaces (1) and (2) shown in Fig. 7.16 and separated by a distance t . An incoming ray making an angle θ with the normal to the plates will be split into the rays AB , CD , EF , etc. The path difference between the wave fronts of two adjacent rays—for example, AB and CD —is

$$\delta = BC + CK$$

where obviously BK is normal to CD . Then†

$$\delta = 2t \cos \theta$$

and for constructive interference to occur

$$n\lambda = 2t \cos \theta \quad (5.1)$$

where n is an integer; Eq. 5.1 is the basic interferometer equation. If the refractive index of the medium between the plates is $\mu \neq 1$, we must modify Eq. 5.1 to

$$n\lambda = 2\mu t \cos \theta \quad (5.1a)$$

Let the parallel rays B , D , F , etc., be brought to a focus by the use of a lens of focal length f as shown in Fig. 7.17. Then when θ fulfills Eq. 5.1a, bright rings will appear in the focal plane, their radius being given by

$$r = f \tan \theta \approx f\theta \quad (5.2)$$

Next we wish to find the intensity of the rings (fringes) and the contrast between bright fringes and background. Let the transmission coefficient be T , and the reflection coefficient be R (for no absorption at the surface $R = 1 - T$); and let the intensity of the incident radiation have an am-

plitude A and therefore intensity I_0 where $I_0 = A^2$. The intensities of the rays that are transmitted through the second surface, B , D , etc., are obtained by squaring their amplitudes. Thus

$$I_B = (AT)^2 = I_0 T^2$$

$$I_D = (A R R' T')^2 = I_0 R^4 T'^2 \text{ etc.}$$

The amplitudes between adjacent rays decrease as t^2 , and, therefore, unless R is close to 1, the interference maxima are not sharp. As R is increased, however, T decreases,† and one might suppose that the intensity of the rings would be greatly diminished; this is not true, since now the amplitudes of many rays can be added. The summation over all amplitudes, taking into account the change in phase, is given by Airy's formula:

$$I_T = \left[\sum_{N=1}^{\infty} A_N \right]^2 = I_0 \frac{T^2}{(1-R)^2} \frac{1}{1 + [4R/(1-R)^2] \sin^2 \delta/2} \quad (5.3)$$

with

$$\delta = 2\pi \frac{2t}{\lambda} \cos \theta$$

We note that at the maxima ($\delta = 0, 2\pi, \dots$)

$$I_T = \frac{I_0 T^2}{(1-R)^2} \quad (5.4)$$

which for no absorption yields $I_T = I_0$; at the minima, ($\delta = \pi, 3\pi, \dots$)

$$I_T = I_0 \frac{T^2}{(1+R)^2} \quad (5.5)$$

which for no absorption yields $I_T = I_0(1-R)^2/(1+R)^2$ showing that for R close to 1, a very good contrast can be achieved. The intensity distribution of the fringes for different values of R is shown in Fig. 7.18, and it is important to note the following points:

- (a) Since the interfering rays emerging from the interferometer are parallel, they must be focused by a lens of good quality (see Fig. 7.17).
- (b) The order of interference n is, in general, very large [$n_0 = (2t/\lambda)$ but the rings that are observed are only from the few orders‡

$$n = (n_0 - \epsilon) - (p - 1) \quad (5.6)$$

where $p = 1, 2, \dots$ may be as high as 10.

† Typical values for a good interferometer are $R = 0.96$; $T = 0.04$.

‡ Equation 5.6 is discussed in Section 5.3.

§ $\delta = BCK = BC(1 + \cos 2\theta) = 2BC \cos^2 \theta = 2t \cos \theta$

hence

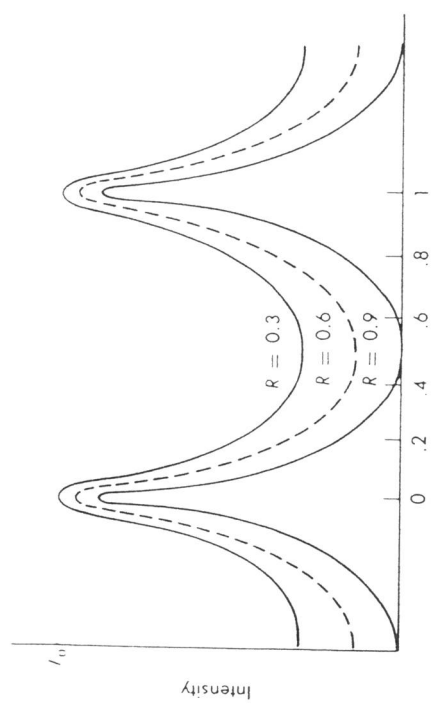


Fig. 7.18 The intensity of light from a Fabry-Perot étalon (viewed in the focal plane of the lens) as a function of radial displacement in units of separation between successive orders. R is the reflection coefficient of the interferometer plates; the contrast improves rapidly for increasing R .

(e) Since interference occurs for rays making an angle θ with the normal to the plates, a perfectly parallel beam may not produce fringes. Since we are interested only in small angles θ , an *almost* parallel beam is allowed to be incident on the interferometer; this is achieved by using an extended source at the focus of the first lens (see Fig. 7.21).

5.2 THE FABRY-PEROT ÉTALON

The multiple-beam interferometer discussed above is easily realized in practice. Two *optically flat* glass or quartz plates with one surface coated with an appropriate reflecting film are used. The plates are assembled in a holder (see Fig. 7.19) and held apart by three very accurately machined spacers. Three spring-mounted screws are used to apply pressure, and by

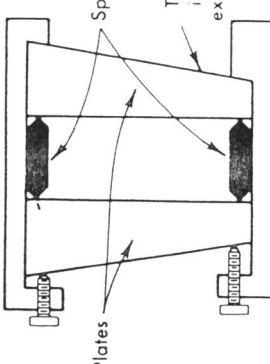


Fig. 7.19 Mounting of the interferometer plates into a Fabry-Perot étalon. Note that the slight slope of the two sides of a plate is usually of the order of 1/10 degree.

careful adjustment, the plates are made parallel. Such an assembly is frequently called a Fabry-Perot étalon.

The plates can be ground flat to $\lambda/20$ (approximately 250 Å), and usually the outer surface is slightly inclined (about 0.1°) with respect to the inner one in order to avoid multiple reflections, which give rise to "ghost" fringes. The reflecting coating is deposited by evaporation in vacuum and is either silver or aluminum depending on the wavelength that will be investigated. Also multilayers of dielectrics are now commonly used. Figure 7.20 gives the reflectivity of these metals as a function of wavelength, but for thick coatings. For thin layers, the reflectivity increases with the thickness of the metal film (but so does the absorption, A); with a film 500 Å thick we may obtain $R = 0.94$, $T = 0.02$, and $A = 0.04$. Note that the performance of the interferometer depends primarily on the quality of these coatings.

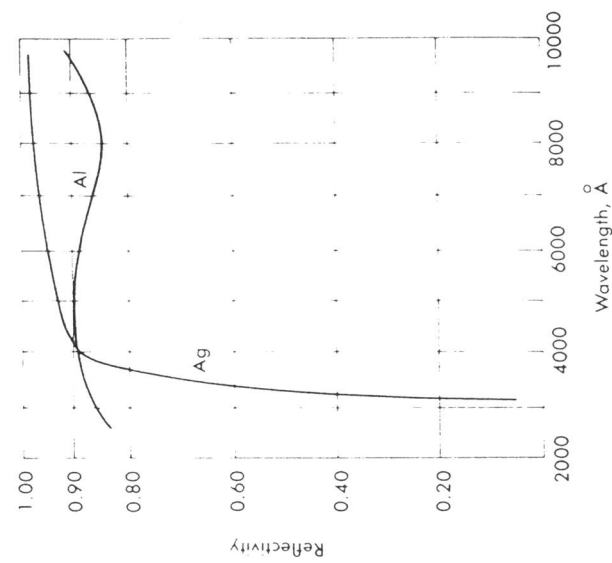


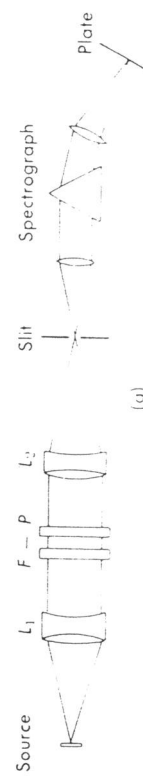
Fig. 7.20 The reflectivity of aluminum and silver coatings as a function of wavelength.

It is also important that the spacers be equal and accurately machined. They can be made of quartz and should also be ground to a $\lambda/20$ precision. It is possible to use several sets of spacers of different length with the same pair of plates; this modifies the spectral range of the étalon, which is given by $\Delta\nu = 1/2t \text{ cm}^{-1}$.

When long exposures are taken, attention must be given to the stability of the system. The air between the plates must be kept at constant tem-

perature in order that the refractive index^f entering Eq. 5.1a does not change; this can be achieved by enclosing the étalon in an insulated box. It is clear that when a source containing several wavelengths, for example, an atomic spectrum, is viewed with a Fabry-Perot, the ring patterns from all wavelengths are superimposed. To separate the patterns and view only the fringes of the line of interest, a low-dispersion spectrometer is used in conjunction with the Fabry-Perot. The ring pattern is focused onto the slit of the spectrometer, in the focal plane of which now appear vertical sections of each ring pattern, but these are dispersed according to the wavelength. We speak of "crossing" the Fabry-Perot with the spectrometer. Good grating spectrographs are occasionally used for that purpose, but a small prism spectrograph is usually adequate. There are basically two methods for introducing the Fabry-Perot étalon in the optical system:

(a) a parallel beam arrangement as shown in Fig. 7.21a, or (b) a converging beam as shown in Fig. 7.21b.



(a)



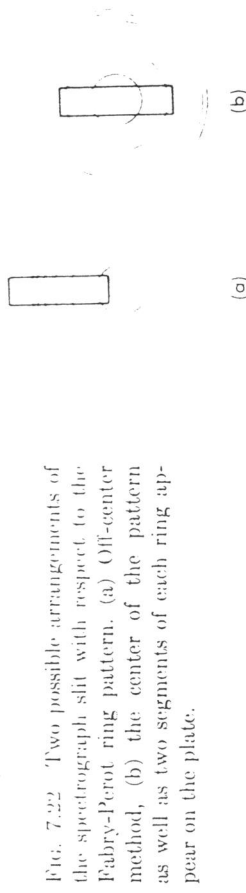
(b)

Fig. 7.21 Two possible arrangements for crossing a Fabry-Perot étalon with a low-resolution spectrophotograph; L_1 and L_2 are compensated lenses and $F-P$ indicates the position of the étalon. (a) The Fabry-Perot is placed in a quasi-parallel beam originating from an extended source. (b) The image of the source is focused onto the Fabry-Perot.

In method (a), lens L_2 focuses the ring pattern onto the spectrometer slit; care must be taken that it be properly adjusted. Maximum light intensity is used with such an arrangement. In method (b), the light source is focused by means of lens L_1 halfway between the Fabry-Perot plates; and the ring pattern is focused by means of L_2 onto the slit. This method has the advantage of easier adjustment of the plates for parallelism and of producing sharper fringes. In both methods the diameter of the rings is

^f The reader may verify that small changes in temperature may shift the ring pattern by a whole fringe.

determined by the focal length of L_2 and the magnification of the spectrograph, which is frequently 1:1 (the ratio of collimator and camera lens focal lengths).



(a)

(b)

Fig. 7.22 Two possible arrangements of the spectrometer slit with respect to the Fabry-Perot ring pattern. (a) Off-center method, (b) the center of the pattern as well as two segments of each ring appear on the plate.

We may project onto the spectrometer slit the central portion of the ring pattern (Fig. 7.22b) or only part of it (Fig. 7.22a). The latter effect can be achieved by tilting the Fabry-Perot étalon (after adjusting the plates) with respect to the optical axis, and leaving the lenses L_1 and L_2 in their original positions. This "off-center" method is used when only a short slit is available, or when the source is so small (not extended) that only few rings can be formed with enough intensity.

5.3 REDUCTION OF THE DATA OBTAINED FROM A FABRY-PEROT

We have seen (Eq. 5.2) that the interference rings formed in the focal plane have radii

$$r_n = f\theta_n \quad (5.2)$$

where the angle θ_n is given by

$$n = \frac{2\mu t}{\lambda} \cos \theta_n = n_0 \cos \theta_n = n_0 \left(1 - 2 \sin^2 \frac{\theta_n}{2}\right) \quad (5.3)$$

and since θ is always small, we obtain

$$n = n_0 \left(1 - \frac{\theta_n^2}{2}\right) \quad \text{or} \quad \theta_n = \sqrt{\frac{2(n_0 - n)}{n_0}} \quad (5.4)$$

Now if θ_n is to correspond to a bright fringe, n must be an integer; however, n_0 , which gives the interference at the center ($\cos \theta = 1$ or $\theta = 0$ in Eq. 5.1), is in general *not* an integer:

$$n_0 = \frac{2\mu t}{\lambda} \quad (5.5)$$

(There is no bright spot in the center of the pattern, in general.) If n_1 is the interference order of the first ring, clearly $n_1 < n_0$ since $n_1 = n_0 \cos \theta_1$. We then let $n_1 = n_0 - \epsilon$, with $0 < \epsilon < 1$ where n_1 is the closest integer to

n_0 (smaller than n_0). Thus, we have in general for the p th ring of the pattern, as measured from the center out,

$$n_p = (n_0 - \epsilon) - (p - 1) \quad (5.6)$$

Combining Eq. 5.6 with Eqs. 5.7 and 5.2, we obtain for the radii of the rings

$$r_p = \sqrt{\frac{2f^2}{\epsilon} \sqrt{(p-1)+\epsilon}} \quad (5.9)$$

We note (a) that the difference between the squares of the radii of adjacent rings is a constant

$$r_{p+1}^2 - r_p^2 = \frac{2f^2}{n_0} \quad (5.10)$$

and (b) that the fraction of an order ϵ can be found by extrapolating to $r_p^2 = 0$ (according to the slope $2f^2/n_0$)[†].

Now,[‡] if there are two components of a spectral line with wavelengths λ_1 and λ_2 , very close to one another, they will have fractional orders at the center ϵ_1 and ϵ_2 :

$$\begin{aligned} \epsilon_1 &= \frac{2t}{\lambda_1} - n_1(1) = 2t\bar{\nu}_1 - n_1(1) \\ \epsilon_2 &= \frac{2t}{\lambda_2} - n_1(2) = 2t\bar{\nu}_2 - n_1(2) \end{aligned}$$

where $n_1(1)$, $n_1(2)$ is the order of the first ring. Hence, if the rings do not overlap by a whole order ($n_1(1) = n_1(2)$), the difference in wave numbers between the two components is simply

$$\bar{\nu}_1 - \bar{\nu}_2 = \frac{\epsilon_1 - \epsilon_2}{2t} \quad (5.11)$$

If the orders are overlapped x times,

$$\bar{\nu}_1 - \bar{\nu}_2 = \frac{x + \epsilon_1 - \epsilon_2}{2t} \quad (5.11b)$$

From Eq. 5.11 we see that we do not need to know t much more accurately than $\epsilon_1 - \epsilon_2$. The fractional order $\epsilon_1, \epsilon_2, \dots$, can hardly be measured to 1/1000; therefore knowledge of t to this accuracy of 1/1000 is amply adequate; this can be easily achieved with a micrometer or a microscope.

[†] See also Fig. 7.28.
[‡] From here on we set $\mu = 1$.

The resolution[†] of the Fabry-Perot can be obtained from Eq. 5.1:

$$\bar{\nu} = \frac{1}{\lambda} = \frac{n}{2t \cos \theta} \quad (5.6)$$

and by differentiation

$$\Delta\bar{\nu} = \frac{\Delta n}{2t} \left[\frac{1}{\cos \theta} - \frac{n \sin \theta}{\cos^2 \theta} \right] \quad (5.12)$$

and since θ is always small

$$\Delta\bar{\nu} \approx \frac{1}{2t} \Delta n \quad (5.13)$$

where Δn is the *fraction of order* by which one ring pattern is shifted with respect to an other. (Note that when this fraction of order is measured at the center, Eq. 5.13 becomes exact, and since $\Delta n(\theta = 0) \approx \epsilon_1 - \epsilon_2$ we get back Eq. 5.11.)

The fraction of order Δn that can be measured experimentally depends on the quality of the plates (as shown by Fig. 5.5, contrast of fringes), on the proper alignment and *focusing* of the optical system, and on the width and relative intensity of the components that are being measured. Values of $\Delta n \approx 1/100$ are common, and with some care this value can be exceeded[‡].

Using $\Delta n = 1/100$, we then find for the resolving power of the Fabry-Perot at a wavelength of $\lambda = 5000 \text{ \AA}$ and a spacing $t = 0.5 \text{ cm}$

$$\frac{\Delta\bar{\nu}}{\bar{\nu}} = \Delta n \left(\frac{\lambda}{2t} \right) = 10^{-2} \times 5 \times 10^{-5} = 5 \times 10^{-7} \quad (5.14)$$

which is quite satisfactory. In general, we see that the wave number interval between adjacent rings (called the free spectral range) is

$$\Delta\bar{\nu} (\text{for } \Delta n = 1) \approx \frac{1}{2t}$$

which can be used as a "scale factor" for the frequency difference of any components appearing in the spectral line.

In reducing the data our aim is to obtain the orders of fractional interference $\epsilon_1, \epsilon_2, \dots$, for all the components of the line, and also to know if any of the components overlap in order, and in that case by how many orders.

[†] See also Eq. 1.5a.
[‡] For example, for the data discussed in Section 6.2, and presented in Fig. 7.27, Δn is of the order of approximately 1/20.

The possibility of components overlapping in order increases when a large spacing is used ($\Delta\bar{v}$ between adjacent fringes is small). To clear up such ambiguity, exposures of the same line are obtained with two or three different sets of spacers, providing also consistency checks of the assignments that were made.

As stated before, we may obtain a Fabry-Perot pattern containing the center of the ring system as shown in Fig. 7.22b. In that case we work with rings close to the center so as to extract the fractional order ϵ for each component. Alternatively, we may obtain a pattern not containing the center as shown in Fig. 7.22a, in which case we use only the p th to the $(p+q)$ th rings; this is known as the off-center method.

We will be concerned with the first method, and let R_p be the radius of the p th ring as measured on the photographic plate. Note that it is possible to measure R_p only if the center of the pattern is included on the plate. The fractional order ϵ is then given by Eq. 5.15 below, which follows from Eq. 5.9

$$\frac{R_{p+1}^2 - R_p^2}{R_{p+1}^2} - p = \epsilon \quad (5.15)$$

We note that the denominator in Eq. 5.15 is a constant, and any adjacent pair of rings can yield a value for ϵ . However, since the squares of the radii of successive rings are linearly related (they form an arithmetic progression) in order to utilize all available information a least squares fit to Eq. 5.15 must be made.

A somewhat less tedious reduction technique, in which the squares of the radii and their differences are tabulated in a square array, is given by Tolansky.[†] Consider a line which has three components a , b , c , and let the respective radii be R_{1a} , R_{1b} , R_{1c} , ..., for component a ; R_{1b} , R_{2b} , R_{3b} , ..., for component b , and similarly for c . From Eq. 5.10 it is clear that the difference between the squares of the radii of component a ,

$$\Delta_a = R_{(p+1),a}^2 - R_{p,a}^2 = \frac{2f^2}{n_{0,a}}$$

is equal (to within a very small part) to the same difference for component b ,

$$\Delta_b = R_{(p+1),b}^2 - R_{p,b}^2 = \frac{2f^2}{n_{0,b}}$$

or any other component of the same line; let these differences be designated

[†] S. Tolansky, *High Resolution Spectroscopy*, Methuen, London, 1947, p. 130.

by Δ . Now from Eq. 5.15,

$$\epsilon_a = \frac{R_{(p+1),a}^2}{\Delta} - p$$

and the required separation (in wave numbers) between the two components, a and b , is

$$\Delta\bar{v} = \frac{\epsilon_a - \epsilon_b}{2L} = \frac{R_{p,a}^2 - R_{p,b}^2}{\Delta} \times \frac{1}{2L} \quad (5.16)$$

If we designate by $\delta_{a,b}^p$ the difference between the square of the radii of the p th order rings of components a and b , and by $\Delta_{p,p+1}^a$ the difference between the square of the radii of the p th and $(p+1)$ th ring of component a , we can form the square array shown in Table 7.4. We note that all Δ 's

TABLE 7.4
SQUARE ARRAY FOR REDUCTION OF FABRY-PEROT DATA

Component	Ring number				
	1	2	3	4	5
a	R_{1a}^2	Δ_{12}^a	R_{2a}^2	Δ_{23}^a	R_{3a}^2
	$\delta_{a,b}^1$	$\delta_{a,b}^2$	$\delta_{a,b}^3$	$\delta_{a,b}^4$	$\delta_{a,b}^5$
	R_{1b}^2	Δ_{12}^b	R_{2b}^2	Δ_{23}^b	R_{3b}^2
b	$\delta_{b,c}^1$	$\delta_{b,c}^2$	$\delta_{b,c}^3$	$\delta_{b,c}^4$	$\delta_{b,c}^5$
	R_{1c}^2	Δ_{12}^c	R_{2c}^2	Δ_{23}^c	R_{3c}^2
	$\delta_{a,b}^1$	$\delta_{a,b}^2$	$\delta_{a,b}^3$	$\delta_{a,b}^4$	$\delta_{a,b}^5$

must have the same value in any one row, and also in any column. Thus when an error in measurement has been made, it becomes immediately apparent, and that radius can be rejected. Similarly all δ 's in one row must be equal and their average can be taken. To obtain $\Delta\bar{v}$, we first obtain the average value of Δ ; however, we should not use every available Δ , but only alternate† ones to obtain the average. Then the average value of the

† Note that if we take

$$\langle \Delta \rangle = (1/k)(\Delta_{12} + \Delta_{23} + \dots + \Delta_{k,k+1})$$

this is equivalent to

$$(1/k)[(R_2^2 - R_1^2) + (R_3^2 - R_2^2) + \dots + (R_{k+1}^2 - R_k^2)] = (1/k)(R_{k+1}^2 - R_1^2)$$

so that only the information from the first and last ring is used.

δ_s is obtained and

$$\Delta\bar{v}_{ab} = \frac{\langle \delta_{ab} \rangle}{2t \langle \Delta \rangle} \quad (5.16a)$$

This method of reduction of the data is quite satisfactory, and use of it will be made in the next section.

For an "off-center" pattern this technique is not applicable, since the radii are not known. The data reduction is based on the fact that now the difference in radii (not in the square of radii) of adjacent rings is almost a constant.[†]

6. The Zeeman Effect of the $\lambda = 5461 \text{ \AA}$ Line of Hg^{198}

6.1 EQUIPMENT AND ALIGNMENT

We now consider the observation in this laboratory of the Zeeman effect on the $\lambda = 5461 \text{ \AA}$ line of Hg^{198} . The choice of the green line is due to its predominance in the mercury spectrum, and the ease with which it can be observed. In an external magnetic field, it is split into nine components, as discussed in detail in Section 2.3. In the present observations, a polarizer parallel to the magnetic field was used, so that only three of the nine components (the π light) appeared. Furthermore, natural mercury exhibits in the green line a large number of hyperfine structure components, and each of them forms a Zeeman pattern. To avoid a multiplicity of components in one spectral line, a separated isotope of mercury was used as the source. Hg^{198} is well suited for our purpose since $I = 0$, and therefore

it exhibits no hyperfine structure; Hg^{198} is usually obtained by neutron capture in gold



and subsequent separation by chemical methods of the mercury from the gold.[†]

The optical system used for this investigation is shown in Fig. 7.23. The Fabry-Perot was crossed in the parallel-beam method with the small constant-deviation spectrograph described in Chapter 2. The étalon and lenses are all mounted on an optical bench to which the spectrograph is rigidly attached. The pair of lenses L_1 forms the light from the source into a parallel beam, while the pair L_2 focuses the Fabry-Perot ring pattern onto the spectrograph slit; the effective focal length of L_2 is 8 cm, and a further magnification of 2 takes place in the spectrograph.

The discharge tube is mounted vertically, as is the spectrograph slit; the slit width was 1 mm. It is clear that in this arrangement not only the ring pattern is focused onto the spectrometer slit but also the image of the source. A sheet of polaroid that could be rotated at will was used as a polarizer.

The spacing of the Fabry-Perot étalon is

$$t = 0.5002 \text{ cm}$$

and it is imperative to adjust the plates carefully for parallelism. This can be done either by viewing through the spectrograph with a frosted glass in the focal plane, and adjusting for the best quality of the pattern, or by a much more sensitive arrangement as shown in Fig. 7.24. A very small aperture (less than 1 mm in diameter) is placed at the position of the source and illuminated with an intense sodium lamp. The Fabry-Perot plates are adjusted to be normal to the optical axis by bringing the image of A reflected by the étalon back onto A . Next, L_3 is adjusted until a series of multiple images of A appears when the observer is located at I ; the plates of the étalon can then be roughly adjusted for parallelism by bringing all

[†] Ready-made Hg^{198} electrodeless discharge tubes can be obtained from the Ryan,

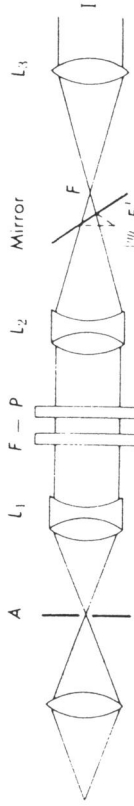


Fig. 7.24 Optical arrangement for aligning a Fabry-Perot étalon. Rough adjustment is made by viewing the image formed by L_3 . Final adjustment is made by viewing the plates from the point F' (or F''). Patterns as shown in Fig. 7.25 will be observed.

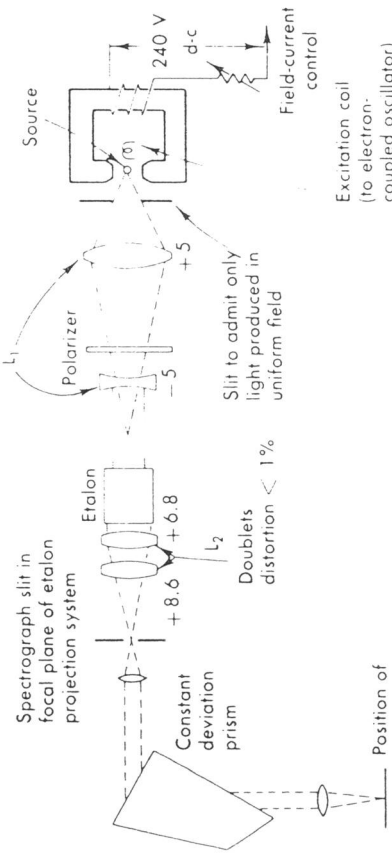


Fig. 7.23 Experimental arrangement used for observing the Zeeman effect with a Fabry-Perot étalon, crossed by a constant deviation prism spectrograph.

[†] G. von Tschirner, loc. cit.

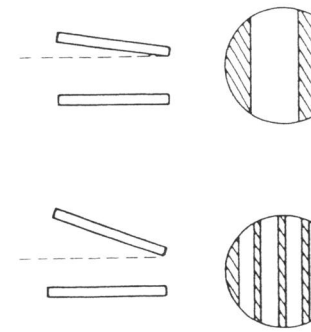


FIG. 7.25 Patterns seen on the axis in the focal plane of a Fabry-Perot when illuminated with a point source. (a) Poor plate parallelism, (b) improved plate parallelism. The tilt of the plates shown is greatly exaggerated.

The diameter of the pole faces was only $1\frac{1}{2}$ in., and a small gap ($\frac{1}{2}$ in.) was used. By tapering the pole faces, higher magnetic fields can be achieved but this reduces the effective area of the field as well as the homogeneity. The magnetic field was measured with a "flip coil" and the calibration of field against current is given in Fig. 7.26. It is seen that field strengths of 12 kilogauss could be reached.

6.2 DATA ON THE ZEEMAN EFFECT

The data presented below were obtained by students†. Figure 7.27 shows the Hg 5461 Å line photographed at various magnet settings. As explained earlier, the source contains a single isotope, and the polarizer allows only the observation of π light. We note that the fringes are rather broad, but it can clearly be seen that when the field is applied the single-line pattern (Fig. 7.27a) breaks up into a triplet, the separation between the components of the triplet becoming larger with increasing field.

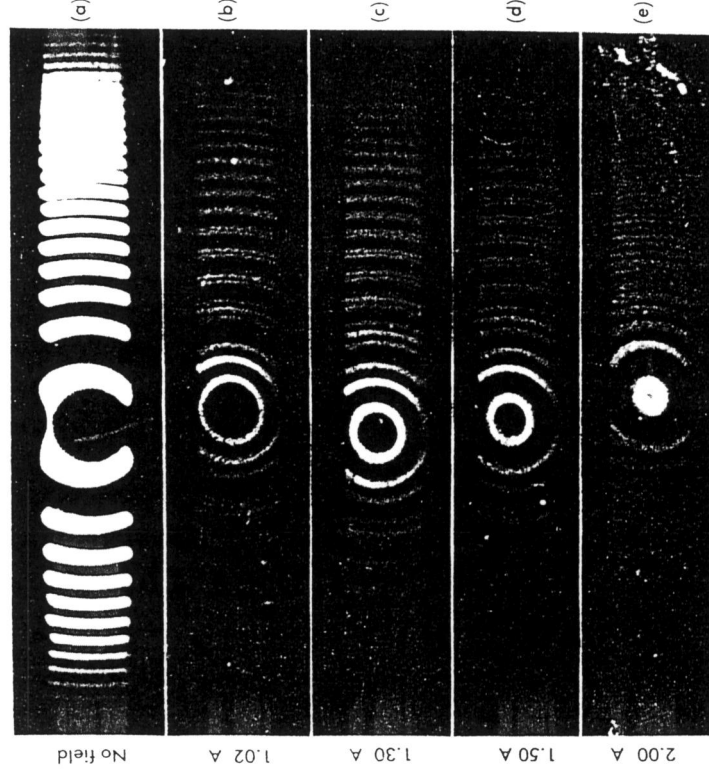


FIG. 7.27 Fabry-Perot patterns showing the Zeeman effect of the green line of mercury. (See the text for additional details.) (a) No magnetic field applied. (b)—(e) A magnetic field of progressively greater strength is applied. Note the splitting of the original line into a triplet of increasing separation.

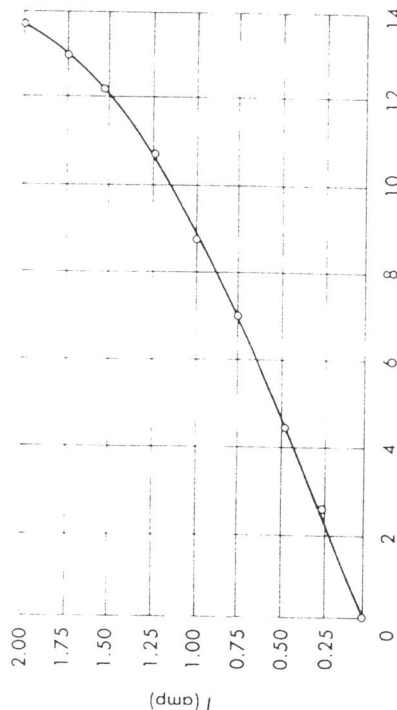


FIG. 7.26 Calibration of the electromagnet used in the Zeeman effect experiment. The magnetic field is plotted against current; note the saturation of the field at high currents.

We will first analyze the exposure with zero field in order to verify that the squares of the radii do indeed follow Eqs. 5.9 and 5.10, and we will find the fractional order at the origin by making a least-squares fit to the squares of the radii. Next we will analyze the 1.00-amp and 1.50-amp exposures by the square-array method.

The initial step in the reduction of the data is the measurement of the diameters (or radii) of the rings. To this effect a traveling microscope was used, and readings were taken directly off the plate; care must be taken to insure that the travel of the microscope is indeed along the diameter of the rings and that the crosshairs are properly oriented. When the fringes in the pattern are as broad as in Fig. 7.27, it is much more accurate to measure the two edges and take the average rather than try to set the crosshairs in the center of the fringe. A more advanced technique for obtaining the ring diameters from the plates is to use a microphotometer.

In Table 7.5 are tabulated the radii of the rings, their squares, and the differences of the squares for the exposure with no field. The same data are also plotted in Fig. 7.28, and it is seen that the straight-line fit is quite satisfactory. The fractional order at the center is found to be $\epsilon_0 = 0.595 \pm 0.024$. For the exposures at 1.00 amp (8.7 kilogauss) and 1.50 amp (12.1 kilogauss), the square array, as described in the Section 5.2, is presented in Tables 7.6 and 7.7; it yields the separation in wave numbers of component a from the central component b , and of c from b . Furthermore, if the fractional order of the central component b is calculated as before, it is found to be $\epsilon_1 = 0.649 \pm 0.024$ and $\epsilon_2 = 0.667 \pm 0.014$, respectively, in

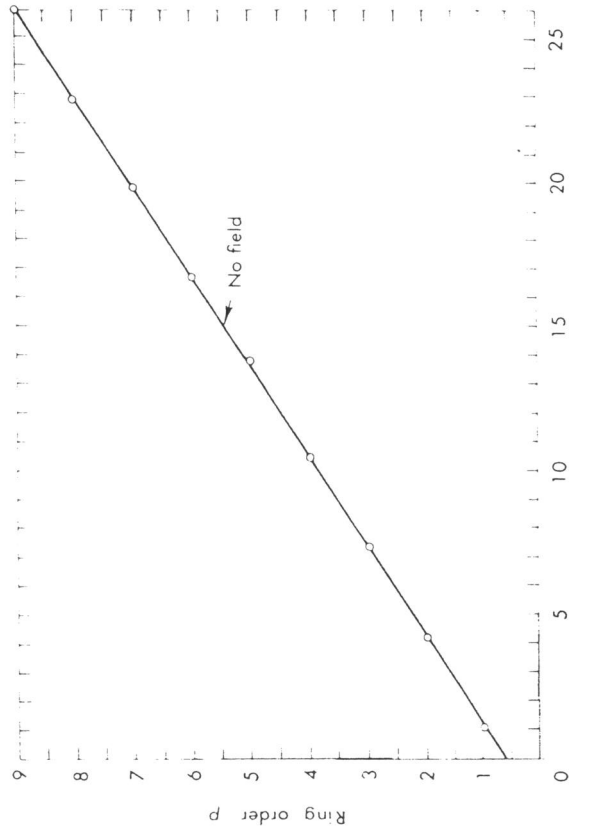


FIG. 7.28 Plot of the square of the Fabry-Perot ring radius against the order of the ring (as measured from the center out). This plot pertains to the data of Fig. 7.27(a) tabulated in Table 7.5 where no magnetic field is applied. The straight line is the least squares fit to the experimental points.

TABLE 7.6
FABRY-PEROT DATA SQUARE ARRAY (FIELD OF 8.7 KILOGAUSS)

Ring order p	Component				
	1	Δ	2	Δ	3
a	0.436	3.136	3.572	3.188	6.740
δ_{ab}	0.625	0.796	0.692	0.838	0.660
b	1.061	3.307	4.368	3.084	7.452
δ_{bc}	0.762	0.650	0.784	0.668	0.524
c	1.823	3.195	5.018	3.218	8.236

Note: All numbers are in mm^2 ; to evaluate $\langle \Delta \rangle$ we used the six numbers between rings 1-2 and 3-4; to evaluate $\langle \delta \rangle$ we used the information from rings 1-4 only. We obtain
 $\langle \Delta \rangle = 3.249$, $\langle \delta_{ab} \rangle = 0.737$, $\langle \delta_{bc} \rangle = 0.716$

and using $t = 0.5002$
 $\Delta\bar{\nu}(a - b) = 0.227 \text{ cm}^{-1}$, $\Delta\bar{\nu}(b - c) = 0.220 \text{ cm}^{-1}$.

TABLE 7.5
RADII OF FABRY-PEROT PATTERN FOR SINGLE LINE

Ring	Radius R_p (cm)	R_p^2 (mm^2)	$(R_{p+1}^2 - R_p^2)$ (mm^2)	Ring R_p (cm)	Radius R_p (mm)	$(R_{p+1}^2 - R_p^2)$ (mm^2)
1	0.103	1.071		7	0.444	1.9758
2	0.205	4.211	3.140	8	0.477	2.995
3	0.271	7.355	3.144	9	0.508	25.857
4	0.323	10.446	3.091	10	0.538	28.944
5	0.370	13.727	3.281	11	0.564	31.866
6	0.408	16.663	2.936	12	0.589	34.692

TABLE 7.7
FABRY-PEROT DATA SQUARE ARRAY (FIELD OF 12.1 KILOGAUSS)

Component	Ring order p				
	1	Δ	2	Δ	3
a	0.207	3.142	3.349	3.411	6.670
δ_{ab}	0.917	0.895	0.858	0.841	2.983
b	1.124	3.120	4.244	3.374	7.618
δ_{bc}	0.921	0.864	0.908	0.806	13.032
c	2.045	3.063	5.108	3.418	8.526
					3.170
					11.696
					3.203
					14.900

Note: All numbers are in nm²; to evaluate $\langle \Delta \rangle$ we used the six numbers between rings 1-2 and 3-4; to evaluate $\langle \delta \rangle$ we used all values except the $\delta_{ab} = 1.031$. We obtain

$$\langle \Delta \rangle = 3.176, \quad \langle \delta_{ab} \rangle = 0.878, \quad \langle \delta_{bc} \rangle = 0.867$$

and using $t = 0.5002$

$$\Delta\bar{v}(a - b) = 0.276 \text{ cm}^{-1}, \quad \Delta\bar{v}(b - c) = 0.273 \text{ cm}^{-1}$$

agreement with the no-field value ϵ_0 . Thus we conclude that the central component is not shifted by the application of the magnetic field.

The final data are summarized in Fig. 7.29 where the spacing of the components against magnetic field is shown. We see that the spacing varies linearly with the field, and the proportionality coefficient has the value

$$\frac{\Delta\bar{v}}{H} = 0.021 \text{ cm}^{-1}/\text{kilogauss} \quad (6.1)$$

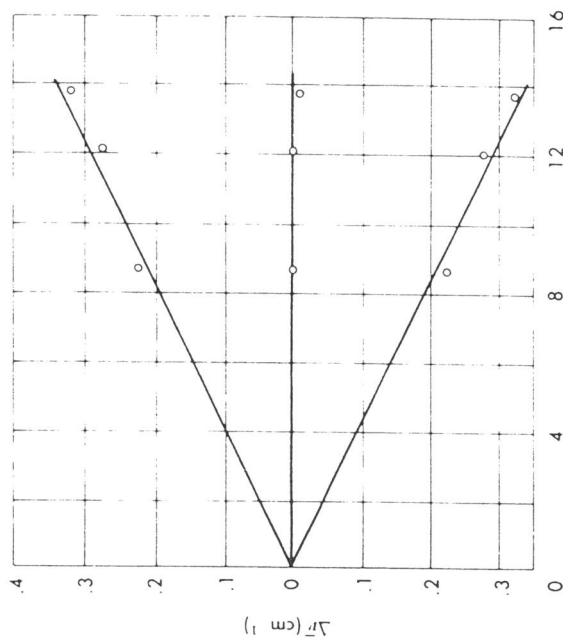
From the discussion of Section 2.3, we know that the Hg 3461 Å line connects the 3S_1 and 3P_2 states; the structure of the line is indicated in Fig. 7.8. Since the polarizer was set to select only components arising in transitions with $\Delta m = 0$, we expect to observe only the three central components, which will be separated by (Eq. 2.16):

$$\Delta\bar{v} = \frac{\mu_0}{hc} (g_i - g_f) H = \frac{1}{2} \frac{\mu_0}{hc} H \quad (6.2)$$

By comparing Eq. 6.2 with the experimental result of Eq. 6.1, we obtain

$$\frac{\mu_0}{hc} = (4.80 \pm 0.5) \times 10^{-5} \text{ cm}^{-1}/\text{gauss}$$

in good agreement with the accepted value



$\Delta\bar{v}$ [cm⁻¹]

B [kilogauss]

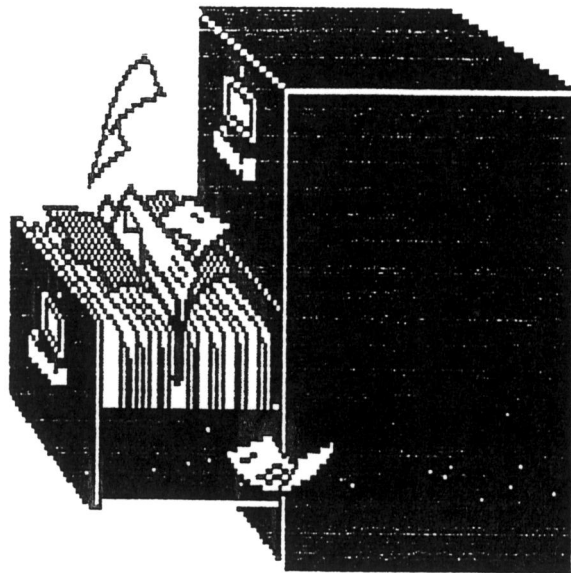
FIG. 7.29 Results obtained on the Zeeman effect of the green line of mercury (see text). The observed displacement of the three components from the zero field value (of the single line) is plotted against magnetic field.

components when the source is placed in a magnetic field. Further, the splitting observed was in excellent agreement with the theory of the anomalous Zeeman effect; the normal Zeeman effect can be excluded, since the energy difference between the components of the line was not $\mu_0 H$ (but instead $\frac{1}{2} \mu_0 H$).

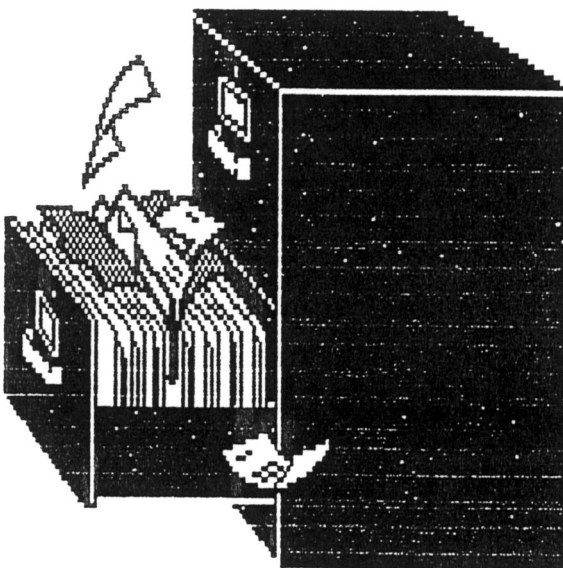
Finally to illustrate the use of the Fabry-Perot in the off-center method, Fig. 7.30 has been included. This exposure was obtained with a high-quality interferometer by Dr. I. C. Bradley III, on the 4047 Å line of Hg¹⁹⁷; the orders shown are from $p = 5$ to $p = 8$. No magnetic field is applied but the hyperfine structure is clearly resolved.



FIG. 7.30 Fabry-Perot pattern of good quality, obtained in the off-center method on the 4047 Å line of Hg¹⁹⁷ (radioactive). The three distinct components observed are due to the hyperfine structure of this



SEPARATOR



REKURUK

FUNDAMENTALS OF OPTICS

Francis A. Jenkins

Harvey E. White

PROFESSORS OF PHYSICS
UNIVERSITY OF CALIFORNIA

Third Edition

INTERNATIONAL STUDENT EDITION

New York Toronto London
McGRAW-HILL BOOK COMPANY, INC.

Tokyo
KOGAKUSHYA COMPANY, LTD.

CHAPTER 29

MAGNETO-OPTICS AND ELECTRO-OPTICS

We have already seen in Chap. 20 and Secs. 23.9, 26.9, and 28.9 that the electromagnetic theory is capable of explaining the main features of the propagation of light through free space and through matter. In further support of the electromagnetic character of light, there is a group of optical experiments which demonstrates the interaction between light and matter when the latter is subjected to a strong external magnetic or electric field. In this group of experiments those which depend for their action on an applied magnetic field are classed under *magneto-optics* and those which depend for their action on an electric field are classed under *electro-optics*. In this chapter the following known optical effects will be treated briefly under these headings:

Magneto-optics

- Zeeman effect
- Inverse Zeeman effect
- Voigt effect
- Cotton-Mouton effect
- Faraday effect
- Kerr magneto-optic effect

The four electro-optic effects in the order listed here are respectively the electric analogues of the first four magneto-optic effects.

29.1. Zeeman* Effect. In the year 1896, Zeeman discovered that when a sodium flame is placed between the poles of a powerful electromagnet, the two yellow lines are considerably broadened. Shortly afterward, Lorentz presented a simple theory for these observations, based upon the electron theory of matter, and predicted that each spectrum line when produced in such a field should be split into two components when viewed parallel to the field [Fig. 29A(a)], and into three components when viewed perpendicular to the field [Fig. 29A(b)]. He further

* P. Zeeman (1865-1935). Dutch physicist and Nobel prize winner (1902). He held numerous honorary positions in scientific circles and is most famous for his work on the splitting up of spectral lines in a magnetic field. His chief contributions are summarized in his celebrated book "Researches in Magneto-optics," Macmillan & Co., Ltd., London, 1913.

predicted that in the longitudinal direction (a) these lines should be circularly polarized and in the transverse direction (b), plane-polarized. With improved experimental conditions these predictions were later verified by Zeeman, Preston, and others in the case of some spectral lines. The Lorentz theory assumes that the electrons in matter are responsible for the origin of light waves and that they are charged particles whose motions are modified by an external magnetic field. In the special case of an electron moving in a circular orbit, the plane of which is

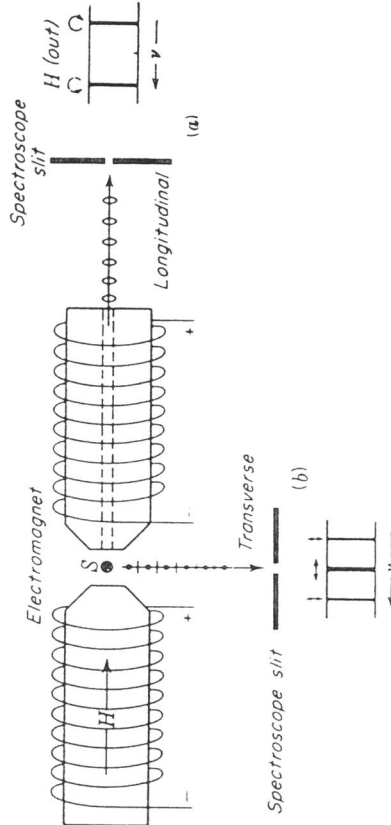


FIG. 29A. Experimental arrangement for observing the Zeeman effect.

normal to the field direction H , the electron should be speeded up or slowed down by an amount proportional to the field strength H . A classical treatment of this problem shows that if ν_0 represents the orbital frequency of the electron in a field-free space, the frequency in the presence of a field will be given by $\nu_0 \pm \Delta\nu$, where

$$\Delta\nu = \frac{eH}{4\pi mc} = 1.40 \times 10^6 \times H \text{ sec}^{-1} \quad (29a)$$

where c is the velocity of light, m the mass of the electron in grams, e the charge on the electron in electrostatic units, and H the magnetic field strength in oersteds.

In the study of spectrum lines this frequency difference $\Delta\nu$ is most conveniently expressed in wave numbers (Sec. 14.14) by dividing by the velocity of light c :

$$\Delta\sigma = \frac{\Delta\nu}{c} = 4.67 \times 10^{-5} \times H \text{ cm}^{-1} \quad (29b)$$

In the classical theory of the Zeeman effect we are concerned with an aggregation of atoms in which the electrons are revolving in circular or elliptical orbits oriented at random in space. It will now be shown,

however, that this situation is equivalent to having one-third of the electrons vibrating in straight lines along the direction of the magnetic field and two-thirds of them revolving in circular orbits in the plane perpendicular to the field. Of the latter ones, half are revolving in one sense and half in the opposite sense. The radius of their orbits is $1/\sqrt{2}$ times the amplitude of the linear vibrations. To prove these statements, let us select any one of the electrons and resolve its elliptical motion into

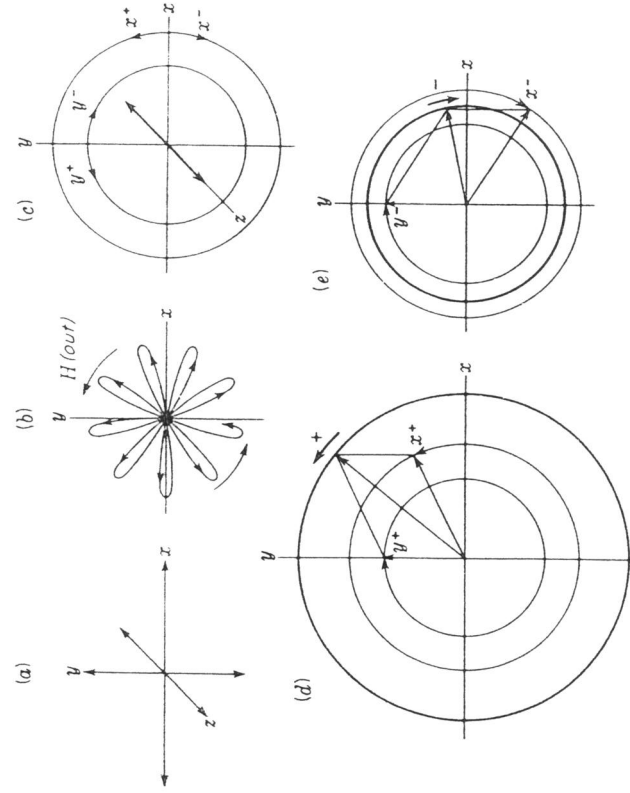


Fig. 29B. Resolution of an orbit for the explanation of the classical Zeeman effect. Under this condition the three components are simple harmonic motions, but for any one electron they are not equal in amplitude nor are they in the same phase.

If a magnetic field is now applied in the z direction, the component parallel to z will be uninfluenced, for it is equivalent to a current directed along the lines of force. The x and y vibrations will each be modified however, since an electron which is moving across a magnetic field

experiences a force

$$F_H = \frac{evH}{c} \quad (29d)$$

perpendicular to the field and also perpendicular to its motion. The effect of this force is to change the x and y components into rosette motions such as that shown in Fig. 29B(b) for the y component. These can be described to better advantage in terms of circular components, y^+ and y^- for the y motion, and x^+ and x^- for the x motion [diagram (c) of the figure]. In the presence of the field both plus circular components have a higher frequency than the minus ones, so we may combine the x^+ and y^+ motions to get a resultant positive circular motion, as in diagram (d), and x^- and y^- to get a negative one, as in (e). Thus the original elliptical orbit when subjected to a magnetic field is equivalent to a linear motion of unchanged frequency along the field, plus two circular motions, one of higher and one of lower frequency, in the plane at right angles to the field.

Only the circular components will emit light along the field direction, and these give circularly polarized light of two different frequencies. The intensity of these two components must be equal when the whole aggregation of atoms is considered, because as the field goes to zero the light is unpolarized. When we observe the light at right angles to the field, we are viewing the circular components edge-on, so these yield two different frequencies of plane-polarized light in which the vibrations are perpendicular to the field direction. Each of them has only half the intensity of the above-mentioned circularly polarized beams. In addition, the linear z motions emit light in the transverse direction. This light has the original frequency ν_0 , vibrates parallel to the field, and has an intensity equal to the sum of the other two. The mean amplitude of the z components for all atoms is therefore $\sqrt{2}$ times as great as that of the x or y components.

Now let us calculate the change of frequency to be expected for the circular components. In the absence of the field the centripetal force on the electron in its circular orbit is furnished by the elastic force, so that by Eq. 29c we have

$$F = -kr = -m\omega_0^2 r \quad (29e)$$

where r is the displacement from the equilibrium position. Under this condition the three components are simple harmonic motions, but for any one electron they are not equal in amplitude nor are they in the same phase.

$$F' = -m\omega^2 r = F \mp F_H = -kr \mp \frac{evH}{c}$$

The positive sign corresponds to a clockwise rotation in the x, y plane and the negative sign to a counterclockwise one. Substituting for $-kr$ its value from Eq. 29e, we then obtain

$$-m\omega^2 r = -m\omega_0^2 r \mp \frac{evH}{c}$$

or, since $v/r = \omega$,

$$\omega^2 - \omega_0^2 = \pm \frac{evH}{mc} = \pm \frac{e\omega H}{mc} \quad (29f)$$

In order to get a simple expression for the change of frequency, it is necessary to assume that the difference in the ω 's is small compared to either ω . This is always justified in practice since it means that the Zeeman shifts are small compared to the frequency of the lines themselves. Then we may put

$$(\omega + \omega_0)(\omega - \omega_0) \simeq 2\omega(\omega - \omega_0)$$

and, from Eq. 22f,

$$\omega - \omega_0 = \pm \frac{eH}{2mc}$$

Since $v = \omega/2\pi$, the change in frequency becomes

$$\Delta\nu = \pm \frac{eH}{4\pi mc} \quad (29g)$$

in agreement with Eq. 29a.

In this derivation it has been tacitly assumed that the radius of the circular motion remains unchanged during the application of the magnetic field. The speeding up or slowing down of the electron in its orbit occurs only while the field is changing and is due to the changing number of lines of force threading the orbit. By Faraday's law of induction this change produces an emf just as it would in a circular loop of wire. The resulting increase or decrease of velocity might be expected to change the radius, but the fact is that there is a corresponding alteration in the centripetal force which is just sufficient to maintain the radius constant. The additional force is that represented by Eq. 29d, which has the same origin as the perpendicular force on a wire carrying a current in a magnetic field.

Let us now summarize what should be the observed effect of a magnetic field on a spectrum line. The result will depend on the direction, with respect to that of the magnetic field, in which the source is viewed. When the source is viewed in the direction of the field, along the z axis, we have what is called the longitudinal Zeeman effect. From this direction only the frequencies $\nu_0 + \Delta\nu$ and $\nu_0 - \Delta\nu$ should appear, and this light

should be right- or left-handed circularly polarized* [Fig. 29C(a)]. Since light is a transverse wave motion, the z vibrations will not emit light of frequency ν_0 in the z direction.

Viewed perpendicular to the field, the z motions should be observed to give plane-polarized light with the electric vector parallel to the field (p components), and the circular motions, seen edge-on, should give plane-polarized light with the electric vector perpendicular to the field (s components). A spectrum line viewed normal to H should therefore reveal three plane-polarized components [Fig. 29C(b)]—a center unshifted line, and two other lines symmetrically located as shown. This is called

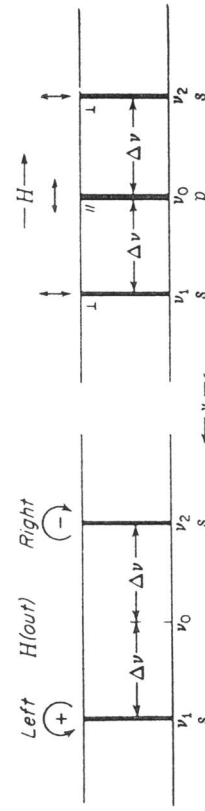


FIG. 29C. Zeeman patterns for a normal triplet, showing the polarization of the light.

a *normal triplet* and is observed for some spectrum lines, though by no means the majority of them.

Since the direction of rotation of the circularly polarized light depends on whether one assumes positive or negative charges as the emitters of light, it is possible to distinguish between these alternatives by using a quarter-wave plate and nicol. Figure 29C(a), where the positive rotation has the higher frequency, was drawn according to our assumption of negative electrons as the emitters.

In Zeeman's early investigations he was not able to split any spectrum lines into doublets or triplets, but he did observe that they were broadened and that the outside edges were polarized, as predicted by Lorentz. The polarization corresponded to emission by negative particles. He was later able to photograph the two outer components of lines arising from the elements zinc, copper, cadmium, and tin, by cutting out the p components with a nicol prism. Preston, using greater dispersion and resolving power, was able to show not only that certain lines were split

* Using the right-hand rule with the thumb pointing in the direction of the field, the fingers point in the direction of the + rotations which have the higher frequency designated by ν_1 . The opposite direction gives the - rotations with the lower frequency ν_2 . Looking against the light, clockwise rotations give rise to right-handed polarized light and counterclockwise rotations give rise to left-handed circularly polarized light. This latter is in agreement with the definitions used in treating optically active substances.

up into triplets when viewed perpendicularly to the field, but that others were split into as many as four, five, or even a much larger number of components. Such patterns of lines, shown in Fig. 29D, are called anomalous Zeeman patterns, and the phenomenon is called the *anomalous Zeeman effect*. The normal triplet separation $2\Delta\nu$ as given by the classical theory is shown by the bracket below each pattern. From Eq. 29a it

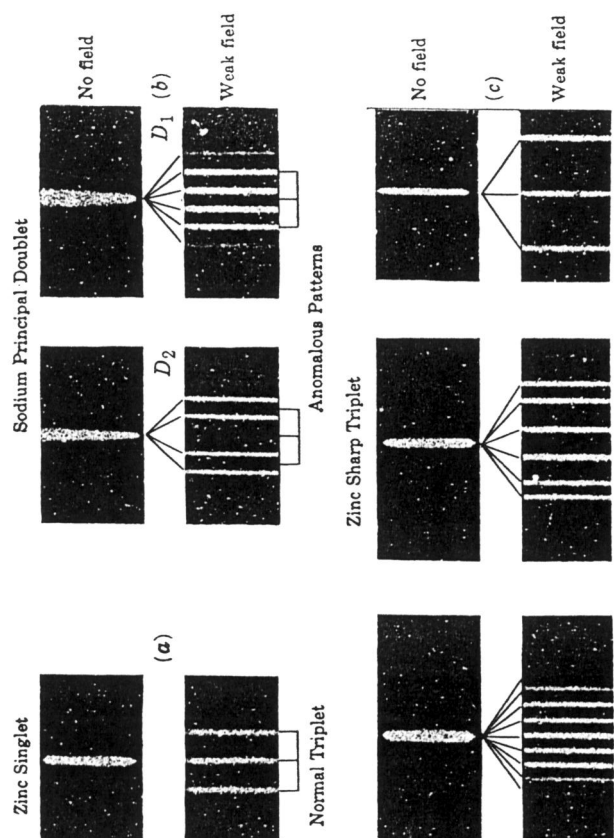


FIG. 29D. Photographs illustrating the normal and anomalous Zeeman effects. It is seen that each of the outer component lines should shift out by an amount proportional to the field strength, thus keeping the pattern symmetrical. In very strong magnetic fields, however, asymmetries are observed in many Zeeman patterns. This phenomenon is known as the quadratic Zeeman effect, although it may also be the beginning of a transition called the Paschen-Back effect according to which all anomalous patterns become normal triplets in the limit of very strong fields. Only the normal triplet can be explained by the classical theory. The more complex patterns are now understood and are in complete agreement with the quantum theory of atomic structure and radiation.*

* For a treatment of the anomalous Zeeman effect, see H. E. White, "Introduction to Atomic Spectra," chaps. 10, 13, and 15, McGraw-Hill Book Company, Inc., New York, 1934.

Each line of an anomalous pattern, when viewed perpendicular to the magnetic field, is found to be plane-polarized. Usually the center lines of a pattern are *p* components with their vibrations parallel to the field H , and those symmetrically placed on either side are *s* components with vibrations perpendicular to the field. In the longitudinal effect only frequencies corresponding to the *s* components are observed, and these are circularly polarized.

The quantum theory has developed to such an extent that one can now predict with the greatest certainty the complete Zeeman pattern for any identified spectrum line in a field of any strength. Conversely, the study of these patterns has become a potent tool in the analysis of complex spectra.

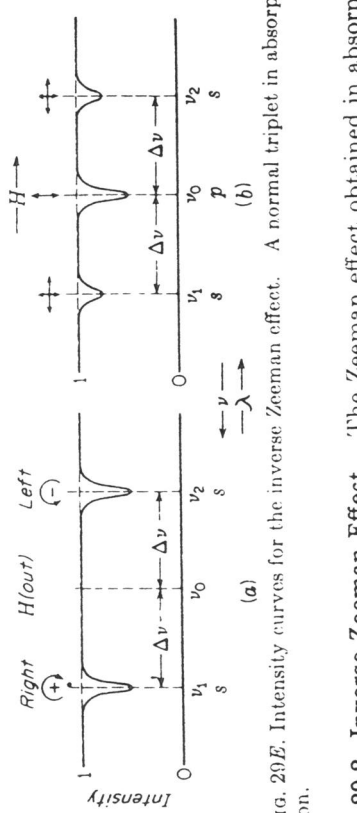
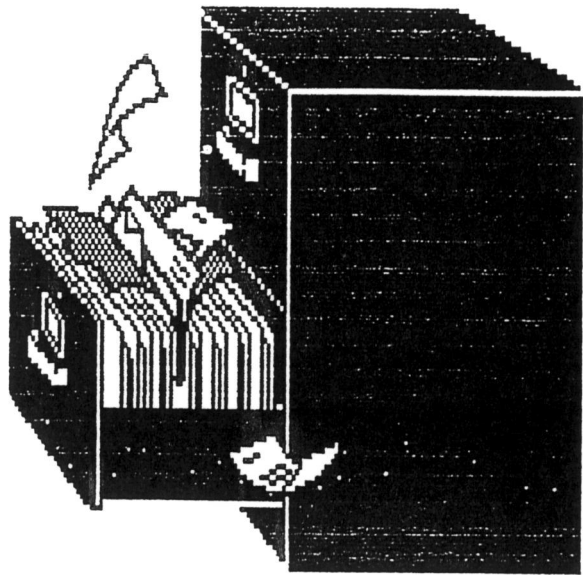
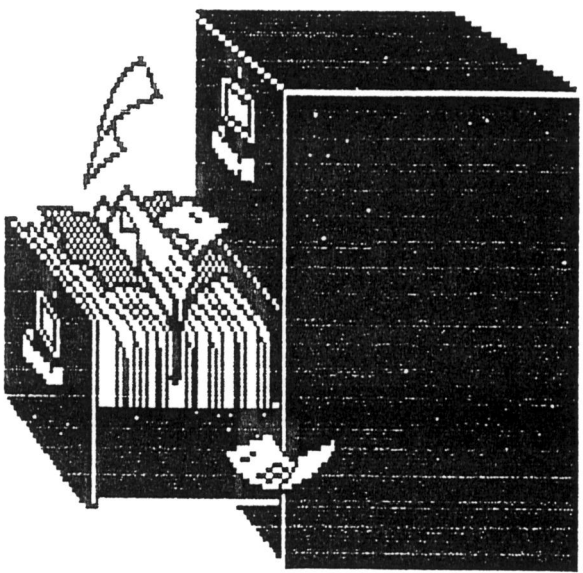


FIG. 29E. Intensity curves for the inverse Zeeman effect. (a) A normal triplet in absorption. (b) An anomalous triplet in absorption.

29.2. Inverse Zeeman Effect. The Zeeman effect obtained in absorption is called the *inverse Zeeman effect*. The phenomenon is observed by sending white light through an absorbing vapor when the latter is subjected to a uniform magnetic field. In considering the longitudinal effect, analogous to Fig. 29C(a), unpolarized light of any particular frequency may be imagined as consisting of right and left circularly polarized components with all possible phase relations. If now ν_0 represents a natural resonance frequency of the vapor in the absence of a field, the plus circular components (see footnote, page 593) of frequency ν_1 will be strongly absorbed in the presence of a field. The corresponding minus circular components of frequency ν_1 pass on through with little decrease in intensity, since to be absorbed these must have the frequency ν_2 . Hence at frequency ν_1 , looking against the field direction as in Fig. 29C(a), right circularly polarized light is transmitted, and for a thick absorbing layer this is one-half as intense as the background of continuous light [Fig. 29E(a)]. A similar argument may be given for ν_2 . The Zeeman components of any spectrum line obtained in absorption along the field direction are therefore not completely absorbed, and the light that does get through is found to be circularly polarized in directions opposite to those of the corresponding components obtained in emission.



SEPARATOR



Experimental Physics for Students

R.M. WHITTELLE

*Senior Lecturer in Physics
The Polytechnic of Central London
and*

J. YARWOOD

*Professor of Physics
The Polytechnic of Central London*



LONDON
CHAPMAN AND HALL

EX 102 J 2 X /4

Results. By the use of three lines of known wavelengths in the photograph of a cadmium spectrum, $\lambda = 6438 \text{ \AA}$, $\lambda = 5086 \text{ \AA}$ and $\lambda = 4678 \text{ \AA}$, the constants in the Equation (5.1) were found to be $\lambda_0 = 636 \text{ \AA}$, $A = 15.586$ and $B = 9.0484$ where λ was measured in centimetres.

Equation (5.1) then becomes

$$\lambda = 2636 + \frac{15.586}{9.0484 + x} \quad (5.2)$$

A photograph of the line spectrum from a mercury discharge lamp is taken parallel to that of the cadmium spectrum on the same plate. The distances x through this spectrum from the line of wavelength 6438 \AA to the lines of various wavelengths are measured. Equation (5.2) is used to determine the wavelengths of these various lines. The wavelengths so found are compared with those listed in the tables of physical constants for the emission spectrum of mercury.

Measured wavelength (\AA)	Listed wavelength (\AA)	Difference
6226	6234	-8
6116	6123	-7
6069	6073	-4
5767	5770	-3
5674	5671	+3
4962	4960	+2
4918	4916	+2
4346	4347	-1
4338	4339	-2
4070	4077	-7
4046	4047	-1

The systematic error is -2 \AA and the random error is $\pm 4 \text{ \AA}$ (Section 1.3).

5.2 Use of an arc source with a constant deviation spectrometer

The constant deviation spectrometer may be used with a source of light in the form of an electric arc source supplied with 50 to 240 V d.c. from a suitable power pack. The electrodes used may be of a variety of metals or carbon. Characteristic line spectra may be photographed using copper or iron electrodes. Carbon electrodes are used to study the line spectra of a number of elements. The element or a suitable salt of the element is placed in the crater of the lower positive carbon electrode. Alternatively, and preferably, the lower carbon rod electrode contains an axial hole through which the material is fed to the arc.

The carbon rod electrodes are contaminated by such a procedure. Ideally, therefore, electrodes should be cleaned in suitable solvents and tested for contamination before any material is placed on them. Otherwise, in the use of the carbon arc for spectrographic analysis, impurities will be present due to the use of previously employed materials.

The presence of elements in a material may often be detected by volatilizing and dissociating the material in a carbon arc, obtaining its line spectrum and identifying it by comparison with the characteristic line spectra known for the elements.

As a multiplicity of lines is often present in the characteristic spectrum of an element and moreover a volatile material may well vaporize quickly in the arc, it is essential to photograph the arc spectrum to obtain a spectrum record which can be examined at leisure because visual observation through the spectrometer telescope would take too long a length of time in identification.

5.3 The Fabry-Perot interferometer

The Fabry-Perot étalon of fixed length used in conjunction with a constant deviation spectrometer gives a method of interference spectroscopy capable in undergraduate experimental work of a very high order of precision in the determination of wavelength and the determination of the fine structure of a spectral line.

Three experiments are described in which are determined (a) the separation between the étalon plates, (b) the wavelength of a spectral line, and (c) the specific charge of an electron by making use of the Zeeman effect.

(a) *The determination of the separation between the plates of a Fabry-Perot étalon.*

The Fabry-Perot étalon is placed on the special mounting between the collimator and the prism of a constant deviation spectrometer. The level and orientation of the étalon can be altered by two adjusting screws without removing the light-tight cover.

The collimator slit is illuminated by light from a cadmium discharge lamp. The telescope shows wide spectral line images intersected by the concentric circular alternately dark and bright Fabry-Perot fringes. It is necessary to measure the diameters of these rings. This may be done either directly with the micrometer eyepiece of the telescope or by replacing the telescope with the camera, and measuring with the travelling microscope the diameters of the rings recorded on the photographic negative. It is of no account that the magnification on taking the photograph may not be unity.

Measurements are best made on the 6438 \AA , 5086 \AA and 4800 \AA lines in the cadmium spectrum. If photographic recording is used, three or four exposures may be made at conveniently spaced separations on the same photographic plate. The red line at 6438 \AA is not so bright as the other two. In order to obtain a reasonably

uniform photographic recording on a panchromatic emulsion, it is therefore best to insert over the collimator slit a red Wratten or Chance light filter of suitable transmission characteristics after the first five seconds or so of the exposure time so that during the latter part of this exposure, light from the other two lines is reduced by absorption in the filter.

The *Benoit method of exact fractions* is used to find the exact length d of the air gap between the glass plates of the Fabry-Perot étalon.

Theory. The basic equation involved in interference of light in a parallel-sided slab of transparent material of refractive index n is

$$2nd \cos \theta = p\lambda$$

where d is the thickness of the slab, θ is the angle of incidence of the light of wavelength λ and p is an integer for constructive interference to occur to give a bright ring around the normal axis.

In the case of the Fabry-Perot étalon, the 'slab' is of air between parallel plates and is taken to have a refractive index n of unity.

At the centre of the interference rings, $\theta = 0^\circ$ so

$$2d = p_0\lambda$$

where p_0 is the order of interference p at the centre. In general there will not be an exact integral number of wavelengths λ within the path d , so p_0 is not an integer.

At bright ring 1, counting from the centre of the pattern, p will be an integer p_1 and the angle θ is denoted by θ_1 . Now

$$2d \cos \theta_1 = p_1\lambda.$$

At bright ring j (where j is an integer), p will be p_j whereas $\theta = \theta_j$ so that

$$2d \cos \theta_j = p_j\lambda$$

Clearly, $p_j = p_1 - j + 1$ (the order p_j is less than p_1 because $\theta_j > \theta_1$ so $\cos \theta_j < \cos \theta_1$).

Therefore

$$2d \cos \theta_j = (p_1 - j + 1)\lambda.$$

As stated, $p_0 = 2d/\lambda$ will not, in general, be an integer. It will, indeed, be p_1 plus some fraction ϵ , i.e.

$$p_0 = p_1 + \epsilon.$$

$$\text{Therefore, } \frac{2d \cos \theta_j}{\lambda} = (p_1 + \epsilon) \cos \theta_j = (p_1 - j + 1)$$

As θ_j is small,

$$\cos \theta_j = 1 - \frac{1}{2}\theta_j^2$$

If D_j is the diameter of the j th ring for wavelength λ ,

$$KD_j = 20_j$$

where K is a constant depending on the magnification produced by either the telescope or the camera lens. Therefore

so that

$$(p_1 + \epsilon) \cos \theta_j = (p_1 + \epsilon)(1 - \frac{1}{8}K^2D_j^2) = (p_1 - j + 1)$$

A graph of D_j^2 against the ring number j is hence a straight line of which the intercept on the j -axis is $1 - \epsilon$ because, when $D_j = 0, j = 1 - \epsilon$.

The fraction ϵ is therefore found for a wavelength λ . For the known wavelengths λ_1, λ_2 and λ_3 , the fractions ϵ_1, ϵ_2 and ϵ_3 are determined in this way. The length d of the étalon is known approximately. For wavelength $\lambda_1, 2d/\lambda_1$ gives approximately the integral part p_{01} of the order p_0 for wavelength λ at the centre. The fractional order ϵ_1 is known from measurements and the graphical procedure described. Therefore $2d$ is apparently $(p_{01} + \epsilon_1)\lambda_1$. However, the integer p_{01} may be incorrect. It is used nevertheless to calculate ϵ_2 for wavelength λ_2 by making use of the relationship

$$\lambda_1(p_{01} + \epsilon_1) = \lambda_2(p_{02} + \epsilon_2).$$

If ϵ_2 calculated in this way differs from ϵ_2 as determined by experiment, then the integers p_{01} and p_{02} are wrong. The procedure is then to take a range of possible integral values of p_{01} all differing by integral values 1, 2, 3 ... 30 say, and $-1, -2, -3 \dots -30$, from the $2d/\lambda_1$ value. At each value allocated to p_{01} in this way, $p_{02} + \epsilon_2$ is recalculated. This is also done for the third wavelength λ_3 . When that integral value of p_{01} is found for which these calculations give ϵ_2 and ϵ_3 (as measured) correct to two significant figures, this value will be the correct one.

The true length of the étalon is then

$$\lambda_1(p_{01} + \epsilon_1)$$

or $\lambda_2(p_{02} + \epsilon_2)$ or $\lambda_3(p_{03} + \epsilon_3)$ which are now all equal.

Results. The lengths of the air gap in the Fabry-Perot étalon is stated to be 10.18 mm nominally, so $2d = 20.36$ mm.

The wavelengths of the three chosen radiations in the cadmium spectrum in air at 20°C , 760 mm Hg pressure with 10 mm Hg water vapour and 0.03% CO_2 present are:

$$\lambda_1 = 6438.5037 \text{ \AA} \text{ for which } \epsilon_1 = 0.22 \text{ (as found by experiment);}$$

$$\lambda_2 = 5085.8483 \text{ \AA} \text{ for which } \epsilon_2 = 0.82;$$

$$\lambda_3 = 4799.9360 \text{ \AA} \text{ for which } \epsilon_3 = 0.30.$$

The order at the centre must be approximately

$$\frac{2d}{\lambda_1} = \frac{20.36}{6438.5037 \times 10^{-7}} = 31600 \text{ approximately.}$$

The following table of values is compiled.